A preliminary study for the high-fidelity DNS of single-phase Pressurised Thermal Shock with buoyancy effects.

Shivang Aggarwal

Technische Universiteit Delft

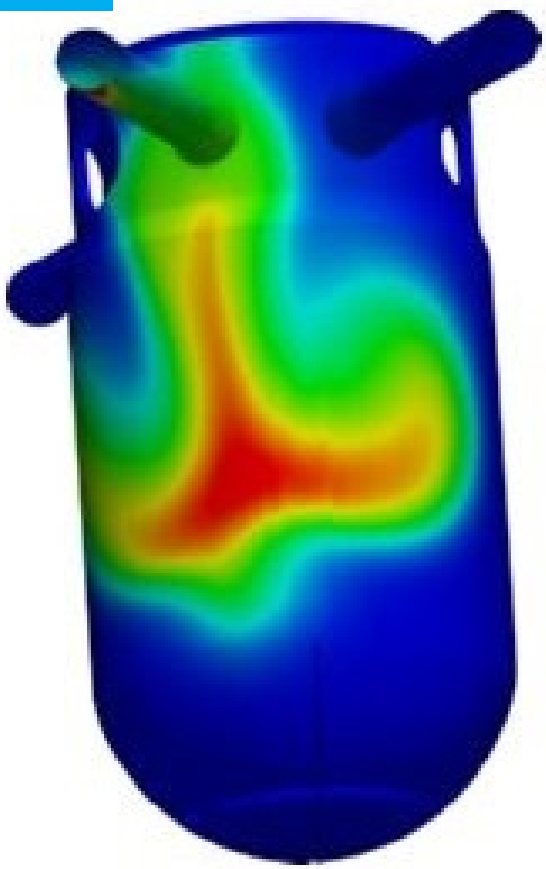

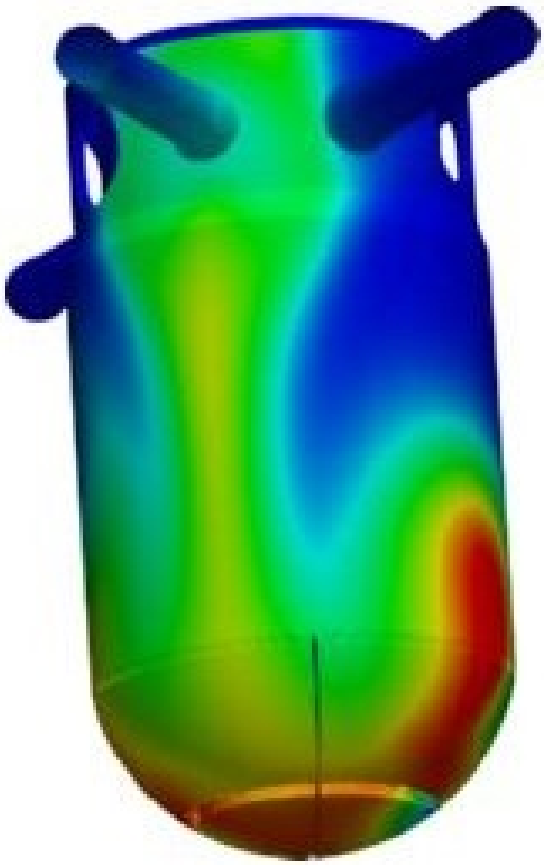

TU Delft Delft University of Technology

Challenge the future

A preliminary study for the high-fidelity DNS of single-phase Pressurised Thermal Shock with buoyancy effects.

by

Shivang Aggarwal

in partial fullfillment of the requirements for the degree of

Master of Science
in Aerospace Engineering,
Specialising in Flight Performance and Propulsion (FPP),

at the Delft University of Technology,
to be defended publicly on Tuesday, December 19th, 2017 at 14.00H .

Student number: **4493966**

Supervisors:	**Dr. Ir. A. Shams,**	**Nuclear Research and Consultancy group (NRG)**
	Dr. Ir. M.I. Gerritsma,	**Aerodynamics, LR Faculty, TU Delft**
Readers :	**Dr. Ir. A.H van Zuijlen,**	**Aerodynamics, LR Faculty, TU Delft**
	Prof. Dr. Ir. L. Veldhuis,	**Flight Performance and Propulsion, LR Faculty, TU Delft**

TU Delft Delft University of Technology

Preface

This is the Master's thesis project report and is a compilation of the work performed for it. The project comes under the domain of nuclear reactor's safety research program and is performed at the Nuclear Research and Consultancy group (NRG) in Petten, The Netherlands. This report will guide through the phenomenon, of interest of this work, which occurs in the nuclear reactor called Pressurised Thermal Shock, the studies performed for it and also the various numerical methodologies which are used to perform the numerical studies.

This thesis project formed the last step of my Master's studies in Aerospace Engineering at TU Delft, and now reflecting back to the time I spent at TU Delft and at the NRG, I find it a great learning experience in terms of both studies and life. I would like to express my sincerest gratitude to Dr. Ir. Afaque Shams, my daily supervisor at NRG, and Dr. Ir. Marc Gerritsma, my university supervisor, for their support and guidance during my project. I have been grateful to receive an opportunity to work on the nuclear research project, although being a student in FPP track. I want to thank Dr. Dante De Santis, with whom I had many discussions, and the other researchers at NRG who were always open to me for their suggestions. I am thankful to my friends for making my experience in the Netherlands exciting and interesting. Lastly, but most importantly, I feel grateful for the unconditional love and support of my family throughout my studies, it wouldn't have been possible without them.

Shivang Aggarwal
Delft, December 2017

Abstract

One of the key components of the nuclear reactor is the reactor pressure vessel (RPV), and its integrity is critical for the safety of the nuclear reactor. Lifetime extension of RPV project deals with the different issues which pose threat to its integrity. One such important issue is the occurrence of pressurised thermal shock (PTS). The most critical PTS scenario occurs during the events of loss of coolant accidents, when the emergency core cooling water is injected to cool down the reactor's core. This cold water mixes with the hot water while descending in the downcomer of the RPV and result in sudden fluctuation in temperature of the vessel wall, giving rise to thermal stresses in it. Thermal-hydraulic codes, which are generally used for the nuclear reactor safety (NRS) applications, are unable to predict this complex 3-dimensional flow mixing phenomenon. Therefore, computational fluid dynamics (CFD) method are considered useful for the comprehensive study of PTS. However, the validation with the experimental data is required to gain trust in predictive capabilities of CFD methods for PTS studies. A high-fidelity direct numerical simulation (DNS) can provide the data for validation. Moreover, it can give more insight about the flow phenomenon and can form a reference database for the turbulence modelling CFD methodologies. The main aim of this thesis project is to perform an extensive preliminary study for the high-fidelity DNS of the single-phase PTS scenario. The objectives are, firstly to design a well defined and well studied numerical case for this DNS, which will be focused towards the buoyancy driven flow mixing in the downcomer of the RPV, and secondly to validate the DNS of a buoyancy driven flow mixing test case. With the help of several simulations, calibration study was performed to find an optimum physical domain and boundary conditions. In addition, a length scales study was performed which will help in mesh estimation for the DNS. Furthermore, a DNS of Rayleigh Bénard convection is performed and the results are compared with the results of a past DNS. This, in total, will contribute to the PTS studies in the direction which has not been dealt in the past and will form an essential basis for the future DNS of the PTS scenario.

Contents

Abstract v

List of Figures viii

List of Figures ix

List of Tables xi

List of Tables xi

1 Introduction 1
1.1 Reactor pressure vessel . . . 1
1.2 Pressurised thermal shock . . . 2
1.3 Thermal-hydraulic analysis . . . 2
1.3.1 Plume cooling . . . 3
1.3.2 Stratification . . . 3
1.4 Experimental study . . . 3
1.4.1 PTS experiments . . . 4
1.5 Requirement of CFD in PTS studies . . . 5
1.6 Route of research program at NRG . . . 6
1.7 Research question of the thesis project. . . . 6
1.8 Description of the thesis report . . . 7

2 Turbulence 9
2.1 Turbulence . . . 9
2.2 Energy cascade . . . 9
2.2.1 Batchelor length scales . . . 11
2.3 Law of wall. . . . 12

3 Governing Equations 15
3.1 Navier-Stokes equation . . . 15
3.2 Boussinesq approximation . . . 15
3.3 Governing equations for Rayleigh Bénard convection (RBC) study. . . . 17
3.3.1 Rayleigh number . . . 17
3.3.2 Prandtl number. . . . 17

4 Numerical Methodology 19
4.1 Reynolds-averaged Navier-Stokes (RANS) equation . . . 19
4.2 Standard k-ϵ turbulence model . . . 19
4.3 Direct numerical simulation . . . 20
4.4 Spatial discretization . . . 20
4.4.1 Finite volume method . . . 21
4.4.2 Spectral element method . . . 22
4.5 Time marching method . . . 25
4.5.1 Explicit method . . . 25
4.5.2 Implicit method . . . 25
4.5.3 Implicit/Explicit Method (IMEX) . . . 26

5 PTS study - without buoyancy effects 29
5.1 Shams et al. study on PTS without buoyancy effects. . . . 29
5.1.1 Physical Domain . . . 29
5.1.2 Boundary conditions. . . . 31
5.1.3 Flow properties . . . 31
5.1.4 Final conclusions of PTS without buoyancy effects study. . . . 31

5.2 Future work prospects . . . 32

6 PTS with buoyancy effects case design 33
6.1 Physical domain . . . 33
6.2 Meshing . . . 35
6.3 Simulation setup . . . 36
6.4 Boundary conditions . . . 36
6.5 Flow properties . . . 37
6.6 Organisation of the work . . . 37
6.7 Cold leg removal . . . 37
6.8 Geometry calibrations . . . 39
6.8.1 Height of the Downcomer . . . 39
6.8.2 Width of the Downcomer . . . 41
6.9 Boundary conditions study . . . 43
6.10 Length scales study . . . 45
6.11 Summary . . . 47

7 Rayleigh Bénard Convection validation study 49
7.1 Rayleigh Bénard convection : importance and significance . . . 49
7.2 Physical domain . . . 49
7.3 Meshing . . . 50
7.4 Cases description . . . 51
7.5 Simulation setup . . . 51
7.6 Nussselt number equations . . . 52
7.7 Results . . . 52
7.7.1 Flow Topology . . . 52
7.7.2 Nusselt number computation . . . 55
7.8 Discussion of results . . . 57

8 Summary and Conclusions 59

Bibliography 61

A Appendix 63
A.1 Reynolds averaging . . . 63
A.2 Statistics . . . 63
A.3 Correlation . . . 64
A.4 Reynolds stress transport (RST) equation . . . 64
A.5 Turbulence kinetic energy . . . 64
A.6 Eddy viscosity hypothesis . . . 65
A.7 Turbulent kinetic energy equation . . . 65
A.8 Nek5000 . . . 65

List of Figures

1.1 Reactor pressure vessel schematic representation, adopted form [1]. 1
1.2 ROCOM Test Facility, adopted from [2]. 4
1.3 Froude number relation with type of flow scenario, density dominated flow ($\diamond$), momentum dominated flow ($\triangle$) and transitional ($\times$). Adopted from [3]. 5

2.1 Energy spectrum for a turbulent flow, adopted from [4]. 10
2.2 Nomenclature for wall-bounded turbulent flows(left) and respective turbulent energy production and dissipation curves(right), adopted from [4]. 12
2.3 Typical velocity profile for turbulent boundary layer, adopted from [4]. 13

4.1 Control volume representation with notation for a 2D grid, adopted from [5]. 21
4.2 Two Lagrange Polynomials based on equi-spaced (left) and GLL points distribution (right), adopted from [6]. 24
4.3 Gauss-Lobatto-Legendre (GLL) points distribution along a single direction inside a super-element for different polynomial order N, adopted form [7]. 25

5.1 Physical domain of PTS Design, adopted from [8]. 30

6.1 Physical domain of PTS Design, finalised by Shams et al. [8]. 34
6.2 Mesh Representation. 36
6.3 Iso-contours of velocity in the cold leg. The velocity is varying between 0 and 1. . . . 38
6.4 Glyphs of velocity in the cold leg showing the velocity magnitude's direction at different point. The velocity is varying between 0 and 1. 38
6.5 Velocity variation at the middle of the cold leg for different Inlet-1 velocity 39
6.6 Time evolution of temperature of flow, at midplane of the downcomer, for different height of the downcomer. Left column is with height (H_2), middle is with height ($H_2 + 3D_p$) and the right column is with height ($H_2 + 6D_p$). 40
6.7 Time evolution of temperature of flow, at midplane of the downcomer, for different width of the downcomer. Left column is with width (W_1, W_2) and right column is with width ($W_1 + 2D_p, W_2 + 2D_p$) 42
6.8 Temperature profile along with the line probe location 43
6.9 Temperature profile at the wall interfaces. 44
6.10 Temperature variation along the line probe for different boundary conditions at time step = 9 sec. 44
6.11 Non-dimensional Kolmogorov length scales. 45
6.12 Non-dimensional Kolmogorov length scales variation along the height of the downcomer. Height varies from top to bottom while moving from left to right in the plot. 46
6.13 Non-dimensional Batchelor length scales. 46
6.14 Non-dimensional Batchelor length scales variation along the height of the downcomer. Height varies from top to bottom while moving from left to right in the plot. 46

7.1 The geometry of the cell. 50
7.2 Spectral elements distribution in xy plan. 51
7.3 Schematic representation of Mesh after grid points generation. 51
7.4 Schematic representation of mean flow arrangement, (- - - - -) for weaker structure, (——-)for most intense structure, adopted from [9]. 53
7.5 Iso-surface of the temperature field for different Rayleigh numbers. Red and blue color represent normalised temperature T = 0.65 and T =0.35 respectively 54

7.6 Iso-surface of the vertical velocity field for different Rayleigh numbers. Red and blue color represents u_z = 0.07 and u_z = -0.07 respectively. 54
7.7 Plots of computed wall and volume averaged Nusselt number for Ra = 10^6. 55
7.8 Plots of computed wall and volume averaged Nusselt number for Ra = 10^8. 56
7.9 Time-averaged Nusselt number, including 95% confidence bounds for Pr = 6.4, Γ =1 for varying Ro and Ra, adopted from [10]. 57

List of Tables

4.1 Coefficients for the k-th order extrapolation (EXTk) schemes with k $\leq$ 3.
For a given k, the coefficients are a_j with 1 $\leq$ j $\leq$ k. Adopted from [6]. 27
4.2 Coefficients for the k-step backward-difference (BDFk) schemes with k $\leq$ 3.
For a given k, the coefficients are b_j with 0 $\leq$ j $\leq$ k. Adopted from [6]. 27

5.1 PTS Design geometric parameter and their description, adopted from [8] 30
5.2 Geometric Dimensions of the selected PTS design,
adopted from [8] 31
5.3 Material properties. 31

6.1 PTS Design geometric parameter and their description. ($*$) represents the difference in dimensions and reason
in dimension from previous configuration, part of it adopted from [8] 35
6.2 Geometric dimensions of the selected PTS design.
(*) represents the change in dimensions from the past study. 35

7.1 Mesh Specifications. 50
7.2 Dimensionless Boundary Condition. 52
7.3 Comparison of the simulations result with Kooij et al. results. 58

List of Abbreviations

BDF	Backward differencing, page 27
CFD	Computational fluid dynamics, page 5
CHT	Conjugate heat transfer, page 37
CV	Control volume, page 21
DNS	Direct numerical simulation, page 6
ECC	Emergency core cooling, page 2
FEM	Finite element method, page 22
Fr	Froude number, page 4
GLL	Gauss-Legendre-Lobatto, page 24
LES	Large eddy simulation, page 5
NRS	Nuclear Reactor Safety, page 5
NRS	Nuclear reactor safety, page 5
Nu	Nusselt number , page 52
Pr	Prandtl number, page 17
PTS	Pressurised thermal shock, page 1
Ra	Rayleigh number, page 17
RANS	Renolds-averaged Navier-Stokes, page 5
RBC	Rayleigh Bénard convection, page 17
Re	Reynolds number, page 9
ROCOM	Rossendorf Coolant Mixing, page 3
RPV	Reactor pressure vessel, page 1
RST	Reynolds stress transport, page 64
SEM	Spectral element method, page 22
TH	Thermal-hydraulic, page 2
TKE	Turbulent kinetic energy, page 9
URANS	Unsteady Reynolds-averaged Navier-Stokes, page 6
WRM	Weighted residual method, page 23

List of Symbols

α	Thermal diffusivity $[m^2/s]$, page 11
β	Thermal expansion coefficient $[K^{-1}]$, page 16
ΔT	Temperature difference between the plates $[K]$, page 17

ϵ	Turbulence dissipation rate $[m^2/s^3]$, page 11
η	Kolmogorov length scale $[m]$, page 11
η_B	Batchelor length scale $[m]$, page 11
κ	Wave number $[m^{-1}]$, page 10
μ	Dynamic viscosity $[N \cdot s/m^2]$, page 15
ν	Kinematic viscosity $[m^2/s]$, page 11
ρ	Density $[kg/m^3]$, page 11
ρ_o	Reference density $[kg/m^3]$, page 16
τ	Kolmogorov time scale $[s]$, page 11
τ_{ij}	Reynolds stress tensor $[m^2]$, page 19
τ_w	Wall shear stress $[kg/(m \cdot s^2)]$, page 12
υ	Kolmogorov velocity scale $[m/s]$, page 11
$\vec{u}$	Velocity vector $[m]$, page 15
C_K	Kolmogorov constant [-], page 11
c_p	Specific heat capacity $[J/(kg \cdot K)]$, page 11
$E(\kappa)$	Energy spectrum $[m^2/s^2]$, page 10
K	Thermal conductivity [W/(m ☐K)] , page 11
k	Turbulent kinetic energy $[m^2/s^2]$, page 10
l_o	Large scales $[m]$, page 9
Re_L	Turbulent Reynolds number [-], page 9
T_o	Reference temperature $[K]$, page 16
u^+	Dimensionless velocity [-], page 13
u_τ	Friction velocity $[m/s]$, page 12
y^+	Dimensionless wall distance [-], page 12
g	Acceleration due to gravity $[m/s^2]$, page 16
H	Distance between the top and bottom of the layer $[m]$, page 17
Pr	Prandtl number [-], page 11
T	Temperature $[K]$, page 15
t	Time $[s]$, page 16
x,y,z	Cartesian directions indices [-], page 16

1

Introduction

This chapter will give a brief background of the research interest and will also discuss the various past findings and experiments conducted for the study of pressurised thermal shock (PTS). Nuclear reactors are widely used around the world for energy production. Owing to the huge risk involved with the handling and use of radioactive materials, nuclear reactor's safety is of critical importance. The lifespan extension program of nuclear power plants involves extensive study on reliability and performance of various components. The integrity assessment of the reactor pressure vessel (RPV) forms one of the essential parts and this project concerns the issue which threatens the integrity of the RPV.

1.1. Reactor pressure vessel

The RPV is a high priority key component as it houses the nuclear reactor core. In fact, it represents the last barrier between the fission products and the containment. It is a cylindrical vessel with a hemispherical bottom, having inlet (also called cold leg) nozzle and a space between the vessel wall and core barrel, called downcomer. The Figure 1.1b shows both of the above-mentioned regions. The cold water is injected through the inlet nozzle to cooldown the reactor's core and this injected water descends in the downcomer. The Figure 1.1a gives a more detailed schematics of the RPV. It is important to mention that this thesis project concerns the flow behaviour in the cold leg and the downcomer.

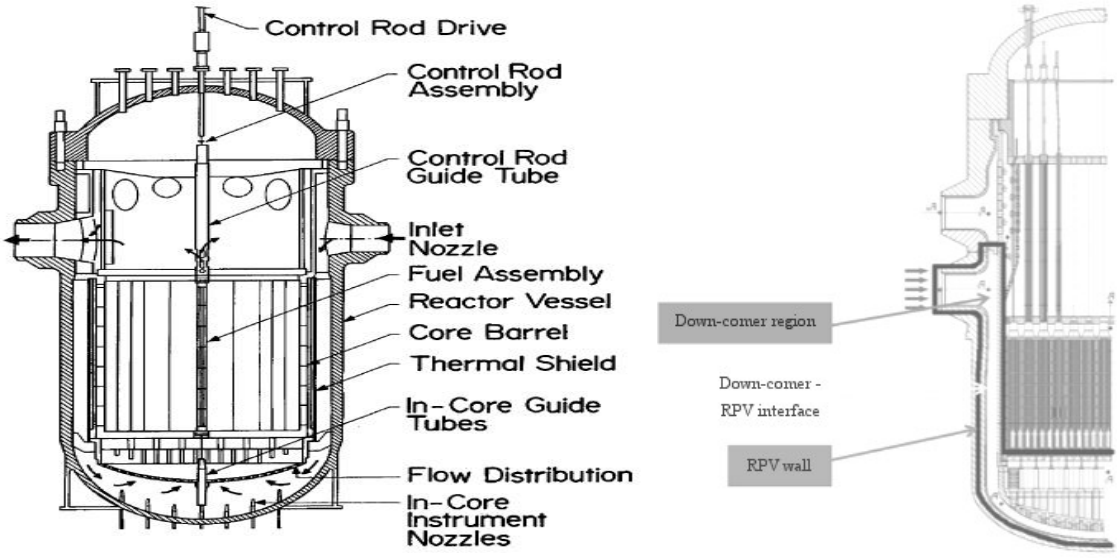

(a) Reactor Pressure Vessel

(b) Downcomer and area of interest

Figure 1.1: Reactor pressure vessel schematic representation, adopted form [1].

1.2. Pressurised thermal shock

In the course of its lifetime, the RPV experiences numerous physical, chemical and mechanical changes. These changes over time are caused by varying loads, flow conditions, corrosion, temperature variations and neutron irradiation. This in turn tests the endurance of materials because of high stress generated in them. The deterioration of mechanical and physical properties is referred to as ageing. The effect of ageing reduces the design margin and leads to forced and early repairs of components, therefore they are considered in design and manufacturing specifications [11]. In addition to ageing, the prolonged exposure to the high neutron flux on the wall of the RPV leads to local embrittlement of the material and welds in the region around the core [12]. These ageing and structural degradation of the RPV can limit the life of the nuclear power plant as it is impossible to replace the RPV.

The embrittled and weakened material under the action of severe transients can generate small crack which can quickly propagate and lead to through-wall cracks, thereby challenging its integrity. One of the severe transients that occur in the nuclear reactor is characterised as pressurised thermal shock (PTS). A PTS denotes the event of rapid cooling of the RPV surfaces and downcomer which occurs in a high pressurised environment. The sudden fluctuations in temperature lead to thermal loads on the vessel. These loads can result in failure of the RPV under the following specific set of conditions [11]:

- An occurrence of reactor transients that subject the vessel to severe thermal shocks.
- An existence of crack or flaws at the inner surface of the vessel wall.
- High enough fast neutron fluence and concentrations of copper and nickel in the vessel wall that reduces its fracture toughness.

The most severe PTS scenario arises during loss of cooling accident (LOCA) event when the emergency core cooling (ECC) water is injected into the cold leg [1]. This cold water first mixes with the already present hot water in the cold leg and then moves towards the downcomer, where further mixing takes place. When the cold mixture come in direct contact with the core barrel wall, it may generate large temperature gradients inside the vessel wall which leads to large thermal stresses. Study of these thermal stresses is crucial for remnant RPV life assessment. Depending on the leak size, its location and the operating conditions of the plant, single-phase flow as well as two-phase flow PTS situations can occur [8].

The PTS scenario's comprehensive study involves following three types of analysis [13]:

- Probabilistic safety assessment : every PTS initiating events are reviewed and are grouped based on similarity in thermal hydraulic nature and frequency. Later the most critical one is selected.
- Thermal-hydraulic (TH) analysis : time evaluation of the fluid temperature distribution and internal pressure, in the vessel, nozzles and downcomer, also the heat transfer coefficient of coolant.
- Probabilistic fracture mechanics : The important data of TH analysis is used. And other vessel specific data are used to calculate the total vessel failure probability for that event.

Downcomer mixing analysis investigates the complex 3-dimensional thermal mixing phenomenon which occurs in downcomer of RPV wall and forms the major part of thermal hydraulic (TH) analysis [11].

1.3. Thermal-hydraulic analysis

Thermal-hydraulic (TH) analysis constitutes the main area of PTS studies where computational fluid dynamics is required for the comprehensive understanding. TH analysis can provide useful data like fluid temperature in the downcomer, the time evolution of temperature and pressure in the downcomer and wall-to-fluid heat transfer for the structural analysis.

When cold water is injected in the cold leg, the cooldown of RPV occurs. But the non-uniform cooling due to a mixing of the cold and hot water in downcomer involves 3-dimensional flow analysis and requires good modelling of the flow behaviour. In these scenarios the one-dimensional system codes fail to produce reliable calculations and therefore, detailed study on the plumes formation and thermal stratification are required.

1.3.1. Plume cooling

When the emergency core cooling water (ECC) is injected in the cold leg, it flows toward the RPV and decents downwards in the downcomer in the form of quasi-planar buoyant plumes because of mixing with hot water. These plumes start to form at the lower edge of the injection nozzle, i.e. at the junction of downcomer and cold leg. These plumes are at locally lower temperature than the background and due to their unsteady behaviour, they can come in direct contact with the core wall leading to thermal stresses.

1.3.2. Stratification

Stratification refers to the variation in the temperature and density in the direction normal to the flow direction. Based on the injection flow speed and density variance the stratification can be perfect or partial. In case of ”perfect stratification,” the denser (colder) fluid will follow as a separate stream sliding along the bottom with a lighter (hot) fluid flowing in the form of a separate stream over the denser fluid [14]. This phenomenon occurs during the ECC injection, where the cold water flows in the form of a strip along the cold leg and falls in the downcomer while being in a direct contact with the hot wall. Thereby, exposing the wall’s flaws and welds to severe cooling and generating thermal stresses.
Partial stratification has attributes of both mixing and perfect stratification. For a well mixed condition sufficient increase in injection velocity is required to break down the injection stream and stable mixing to occur [15].

1.4. Experimental study

For performing experimental simulations of realistic scenario which occur in the nuclear reactor, Rossendorf Coolant Mixing (ROCOM) test facility operated at Forschungszentrum Dresden-Rossendorf (FZD) was chosen. The edging feature of this facility is its high flexibility in choosing boundary conditions and ability to perform measurement with highest spatial resolution. This makes it suitable for performing mixing experiments aimed at turbulent flow mixing in downcomer [2]. Various tests with different flow conditions were performed. In this study, experiments performed for the study of PTS scenario will be briefly discussed.

At ROCOM facility, the mock-up of RPV is made of perspex (glass) which allows visualising the mixing occurring in the downcomer. It consists of four inlet and four outlet nozzles. The model incorporates important details of an actual RPV which are important for coolant mixing like nozzles, vessel wall, core barrel wall and downcomer but with a linear scaled dimension of 1:5. The Figure 1.2a showcase the schematic drawing of ROCOM’s RPV model with dimensions and details of sensor locations. The Figure 1.2b shows the RPV model where the location of nozzles and structure can be observed. With detailed modelling of inlet nozzles, segments and controllable individual pumps for inlet and exit, it is possible to simulate the desired scenario. The facility is operated with water at room temperature and ambient pressure [2].

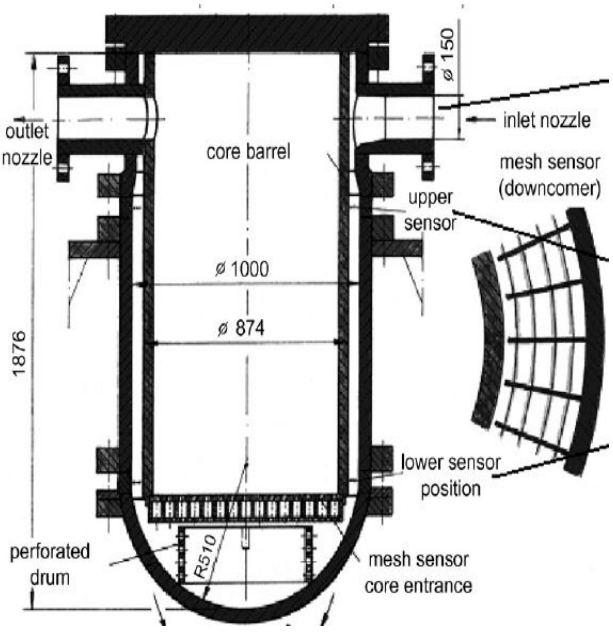

(a) Dimension of Experimental setup
All dimensions are in mm

(b) Model of Reactor Pressure Vessel (RPV) at ROCOM facilty

Figure 1.2: ROCOM Test Facility, adopted from [2].

1.4.1. PTS experiments

The flow mixing occurring in the downcomer can be momentum driven or buoyancy driven. In case of buoyancy driven, due to the difference in density the dominant buoyancy forces dictates the motion of the fluid. When the injection velocity is higher, the momentum effect dominates the density effects. For simulating the buoyancy driven flow it is very important to keep the injection velocity within certain limits. Due to the fact that the facility cannot be heated, the necessary density difference was achieved by adding sugar (glucose) in the cold ECC water. Since the viscosity difference becomes large only at a concentration higher than the one required (10%) for the experiment, the method was found to be acceptable. For the buoyancy driven flow, the density difference should be considerable. The exact knowledge of the spatial distribution of ECC water in downcomer is important for the PTS study [16].

By varying the density between 0 and 10% several experiments were performed. The goal was to find the condition for transition between momentum and buoyancy driven mixing and also to investigate the influence of density difference on mixing in the downcomer.

Without density differences, momentum-driven due to injection velocity, the flow upon entry in the downcomer splits into two streams and flows in right and left forming a helix around the core barrel circumferentially which join together at the opposite side of the entry and move downwards later on. Whereas in case of 10% density difference the stratification was observed. And the density difference partly suppresses the splitting of stream and propagation in the circumferential direction. The injected cold water falls down in almost straight streamline to reach the bottom of the vessel [16]. When the density difference was 4%, a transition between momentum and the density-driven case was observed. The flow behaviour was the combination of both circumferential propagation and streamline descend in the downcomer which shows the effect of both driving mechanisms.

In a separate experimental study conducted in the past [3], the difference between density and momentum driven flow mixing was observed. And it was related to the Froude number (Fr) , calculated using inlet conditions and downcomer (see Equation (1.1)). The Figure 1.3 shows the above-mentioned types of flow scenarios such as: density dominated flow ($\diamond$), momentum dominated flow ($\triangle$) and transitional ($\times$).

$$Fr = \frac{v_{in}}{\sqrt{g.s.\frac{\rho_{in}-\rho_a}{\rho_{in}}}}, \tag{1.1}$$

here v_{in} is the velocity at the inlet, g is the gravitational acceleration, s is the height of the downcomer, ρ_{in} the density of the incoming flow, ρ_a the density of the ambient water in the downcomer. It was found that all the density driven experiments are on the left of Fr = 4.0 isoline whereas the momentum driven are on right of Fr = 7.0 isoline. The region between Fr = 4.0 and Fr = 7.0 is the transition region. Normalized ECC density is the ratio of incoming water's density to ambient (already present) water in downcomer density.

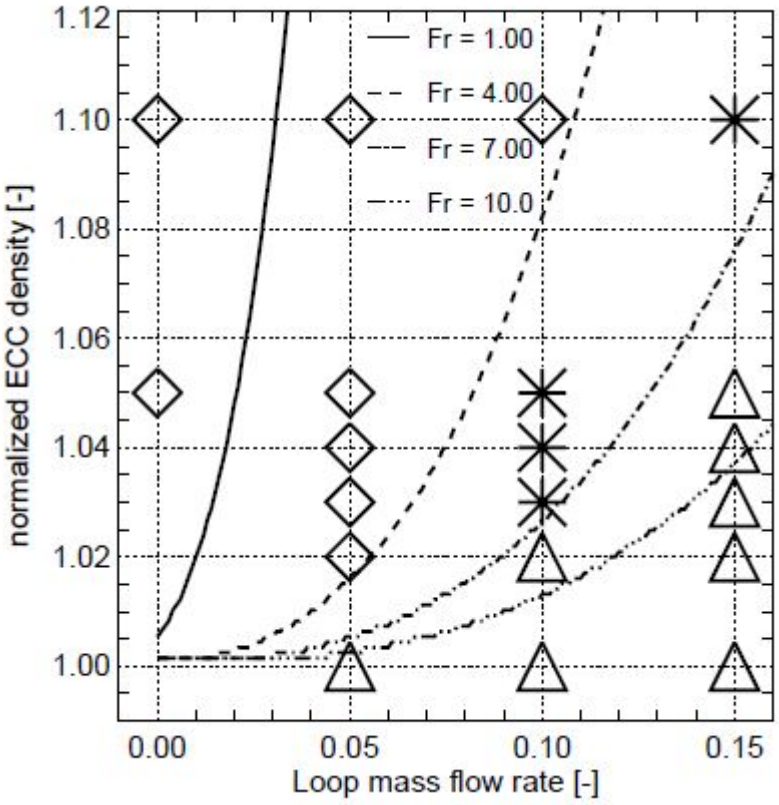

Figure 1.3: Froude number relation with type of flow scenario, density dominated flow (⋄), momentum dominated flow (△) and transitional (×). Adopted from [3].

1.5. Requirement of CFD in PTS studies

Computational fluid dynamics (CFD) is considered a more reliable way, which can prove critical in predicting the flow phenomena. But it is necessary to perform an extensive validation program to gain trust in the CFD modelling for the PTS. In the past, traditional thermal-hydraulic system codes had been employed for nuclear reactor safety related studies. As these codes are based on simplified one-dimensional flow representations, they are not capable to reliably predict the complex 3-dimensional flow phenomenon which occurs during the ECC injection [8]. Therefore, PTS is considered as one of those NRS project where CFD can prove useful in terms of better understanding, quantification and improved safety estimation [1].

Several CFD simulations had been performed for the selected ROCOM experiments [17]. It was found that the transient Reynolds-averaged Navier-Stokes (RANS) simulation is capable to accurately predict the thermal stratification which occurs in the cold leg. But, it had the limitation in capturing the complex mixing phenomena which occur in the downcomer of the RPV [18]. It was also observed that large eddy simulations (LES) are capable to reproduce the complex flow phenomenon which occurs during ECC mixing experiment at the ROCOM facility [19]. CFD studies done at test facility using CFX and employing standard $k-\epsilon$ turbulence model, were found to be capable of reproducing most of the measured results for the single phase mixing scenarios, as long as density effects were absent [16]. There are limitations of the experiments in measuring all the relevant data, like 3-dimensional

velocities, and capturing all important phenomena occurring in RPV during ECC events. For example, as the wall of the vessel at ROCOM was made of acrylic glass, no heat transfer data were obtained from the experiments. Also, the spatial resolution in the region close to the wall was limited, leading to insufficient data of velocity and temperature fluctuations in those regions [8]. These data are important for computing the wall heat flux. Direct numerical simulation (DNS) databases form a valid alternative for the reference and overcoming the limitations of experiments. It can help in obtaining the complete characterisation of all flow and heat transport phenomena. Such a database can be used as a reference for validating the turbulence modelling methods like unsteady Reynolds-averaged Navier-Stokes (URANS), LES and Hybrid (LES/URANS). However, some simplification in the complex geometry of RPV is required to make it feasible for the DNS.

1.6. Route of research program at NRG

At NRG, an extensive research program is underway with a goal to make a DNS database for the single-phase PTS flow scenario which requires a high-fidelity DNS computations. Realistic PTS scenario involves buoyancy driven mixing of flow and formation of thermal plumes. Single-phase PTS scenario exhibits the co-occurrence of various complex phenomenon including T-junction type of turbulent thermal mixing, thermally stratified flow and buoyancy-driven plumes formation. As a first step, the design of a numerical experiment for the PTS without buoyancy effect was conducted, which is discussed in the Chapter 5. This step involved the design of a PTS configuration, performing DNS with third, fifth and seventh order accuracy in space (for spectral element method) successively. The third order accuracy provides the initial cross-check of the design and help in learning the flow physics and statistical convergence. The fifth order accuracy will be an under-resolved DNS but a step closer to the true DNS. The seventh order will be a high-quality DNS and will conclude this step. This in-total concluded the PTS without buoyancy study and provides a basis for the next step i.e. PTS with buoyancy effect. The second step's goal is to perform a high-quality DNS of single-phase PTS with buoyancy effects moving in a similar fashion as the previous step. This thesis project comes under the work related to the above-mentioned second step, i.e. PTS with buoyancy effects.

1.7. Research question of the thesis project.

The background, relevance, the past experimental studies and the flow phenomena of the PTS scenario is already discussed in this chapter, therefore we can outline the research questions of this thesis project as

- To design an optimum numerical case for the single-phase PTS scenario, with emphasis on buoyancy driven flow mixing in the downcomer, which will be feasible for the direct numerical simulation (DNS).
  - This will require the study of boundary conditions, geometrical configuration and flow parameters for the transient flow mixing in the downcomer, which will be performed with the help of several URANS simulations. And later finalising the most feasible ones, which will require less computational time while still keeping the important aspects of the actual scenario of concern.
- Assessment of Nek5000 with buoyancy driven flow mixing test case.
  - The main goal of the PTS project at NRG is to create a DNS database, which will be achieved by performing a high-fidelity DNS of the case finalised in the above-mentioned step. The Nek5000 code is chosen to perform this task. As the DNS of final PTS case will be large and will require huge computational time, it becomes essential to perform a detailed study of buoyancy-driven flow mixing scenario, using Nek5000, for a smaller case, prior to moving towards the DNS of complicated geometry and flow conditions. For this task, a well-known and extensively studied case of Rayleigh Bénard convection (RBC) is chosen. A numerical study of RBC was performed by Kooij et al. [10] using Nek5000 in the past. And the results of this DNS can provide a proper comparison for the validation.

1.8. Description of the thesis report

In this chapter, the background and importance of the PTS are discussed. Also, the important areas of concern like plume formations, downcomer mixing and stratification were explained. The Chapter 2 will give an overview of turbulence and the concept of energy cascade. As the flow mixing in PTS scenario is turbulent phenomenon, therefore, the background of important things which deals with this project is explained here. In Chapter 3, we will discuss the important governing equations which are used in this thesis project and the motivation and reasoning behind selecting them. In Chapter 4, the numerical methodologies used are discussed briefly. In the Chapter 5, past work done for the PTS without buoyancy effects is summarised. This will be followed by the Chapter 6 which discuss the study performed on the PTS with buoyancy effects and the findings of the simulations. The Chapter 7 discuss the validation study performed for the Rayleigh Bénard convection (RBC) case.

2

Turbulence

Both PTS and Rayleigh Bénard convection (RBC), areas of interest of this project, involves turbulent flow mixing and therefore it is important to have a brief background of the turbulence before moving to discussion of the simulations and their results. For the PTS and RBC numerical simulations, appropriate mesh selection was necessary which required study of the Kolmogorov and Batchelor length scales. This chapter will discuss the different scales and layers involved in any turbulent flow scenario and their importance.

2.1. Turbulence

Turbulence is one of those complex phenomenon which is omnipresent in nature and surrounding activities. It occurs almost in every situation in which fluids are involved. It can be observed in the flows through nozzles, turbomachinery, heat exchangers and in case of flow around the moving objects like aircraft, also atmospheric phenomena are driven by turbulence.
Turbulence is a 3-dimensional and time-dependent phenomenon. Therefore, a huge amount of data is required for the complete description of the turbulent flow. It is characterised by the presence of eddies of different size and orientation, which drives its chaotic and unsteady behaviour. Turbulence always occurs at high Reynolds number, and it develops as an instability to laminar flow [4]. These instabilities are attributed to the interaction between the viscous and inertial term of the Navier-stokes equations. At high Re, the Navier-Stokes show extreme sensitivity to disturbances and turbulence is the response of these disturbances [4].

2.2. Energy cascade

Large eddies are characterised by the length scale (l_o) which is comparable to the flow length scale and similarly their characteristic velocity is comparable to the flow velocity. Therefore, the Reynolds number associated with these eddies is of the order of flow Reynolds number and hence, the effect of viscosity on these eddies is negligibly small. Reynolds number associated with the large eddies is referred as turbulent Reynolds number (Re_L) and is defined as

$$Re_L = \frac{k^{1/2} l_o}{\nu} = \frac{k^2}{\epsilon \nu} \tag{2.1}$$

The turbulence features energy cascading, i.e. the process by which the turbulent kinetic energy (TKE) created by large eddies is transferred to the smaller eddies, which further breaks up and transfer the energy to yet smaller eddies. This transfer of energy take place until the Reynolds number associated with the smallest eddies is sufficiently small for the stable eddy motion and the molecular viscosity is effective in dissipating the kinetic energy. At these scales, kinetic energy is converted into heat. The physical mechanism behind this transfer of energy is vortex stretching. The large scales are primarily inviscid whereas the small scales are dominated by viscosity.

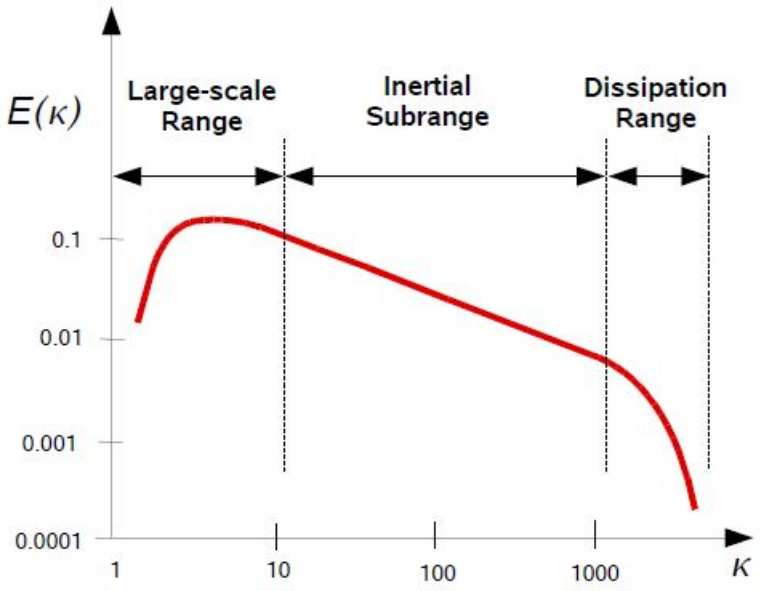

Figure 2.1: Energy spectrum for a turbulent flow, adopted from [4].

Different ranges of the scales can be shown using wave number, κ which is defined as

$$\kappa = \frac{2\pi}{l}, \tag{2.2}$$

where l is the length scale of the eddies.
So, in essence, with the increase in the length scale, the wave number decreases and vice versa. The turbulent kinetic energy distribution among the eddies of different sizes can be represented using energy spectrum. Energy spectrum, $E(\kappa)$, is the energy contained in the eddies with scale size l and wave number, κ. Therefore, the turbulent kinetic energy,k, contained in the eddies with wave number between κ_a and κ_b will be

$$k = \int_{\kappa_b}^{\kappa_a} E(\kappa) d\kappa. \tag{2.3}$$

The Figure 2.1 shows the plot of E(κ) vs κ for a turbulent flow. It can be observed that the large scale range contains most of the energy where the production occurs.

In universal equilibrium theory of Kolmogorov [20, 21], the concept of scale separation is discussed which is based on assumption that the small scale's dynamics are statistically independent of those of the large scales. Therefore, the behaviour of small scales is determined by the energy transferred to them by large scales through cascade and kinematic viscosity. In case of the equilibrium state of turbulent flow, the rate of energy supplied by large scales will be equal to the energy dissipated by small scales. The scales are divided into three regions as

- **Large scale range** : These scales are responsible for turbulence production and carry the major portion of turbulent kinetic energy. They take the energy from the mean flow and are subjected to the macroscopic effects of geometry and force. Therefore, study of this range is important for the evaluation of forces and moments to understand the major flow behaviour.

- **Inertial subrange** : In case of sufficiently high Reynolds number, this range of scales will exist and form the bridge by assisting in energy transfer between the large and the smallest scales, with negligible dissipation of energy. In this range, the energy spectrum is defined as

$$E(\kappa) = C_K \epsilon^{\frac{2}{3}} \kappa^{-\frac{5}{3}}, \tag{2.4}$$

where C_K is Kolmogrov constant and κ is the wave number.

- **Dissipation range**: In this range, the behaviour of eddies is dominated by the viscosity, ν, and the rate of energy transferred from the large scales which is known turbulence dissipation rate, ϵ . The smallest eddies present in the flow are known as Kolmogorov scales and are indicative of the scales at which the dissipation occurs. The expressions for length, velocity and time scale are as follows :

  Kolmogorov length scale :

$$\eta \approx \left(\frac{\nu^3}{\epsilon}\right)^{\frac{1}{4}}. \tag{2.5}$$

  Kolmogorov time scale:

$$\tau \approx \left(\frac{\nu}{\epsilon}\right)^{\frac{1}{2}}. \tag{2.6}$$

  Kolmogorov velocity scale :

$$\upsilon \approx \left(\nu\epsilon\right)^{\frac{1}{4}}. \tag{2.7}$$

Small and large length scales are related to the turbulent Reynolds number (Re_L) as [4]

$$\frac{l_o}{\eta} \approx Re_L^{3/4}, \tag{2.8}$$

In the expression (2.8), as the ratio l_o/η increases with increase in Reynolds number there will be larger range of intermediate eddies with the scale between l_o and η .

2.2.1. Batchelor length scales

For the flow scenario involving heat transfer, Kolmogorov scales may not be smallest scales to describe the involved process. Similar to momentum diffusion the thermal diffusion occurs at the smallest scales called Batchelor length scales, η_B. The relation between the thermal diffusivity and molecular diffusivity is defined by Prandtl number, Pr , and therefore the Kolmogorov and Batchelor length scales can be related as

$$Pr = \frac{\nu}{\alpha}, \tag{2.9}$$

where

$$\alpha = \frac{K}{\rho c_p}, \tag{2.10}$$

Therefore,

$$\eta_B = \left(\frac{\alpha^2 \nu}{\epsilon}\right)^{1/4} \quad \text{for} \quad Pr > 1, \tag{2.11}$$

$$\eta_B = \left(\frac{\alpha^3}{\epsilon}\right)^{1/4} \quad \text{for} \quad Pr < 1, \tag{2.12}$$

where ν is viscosity, α is thermal diffusivity, K is thermal conductivity and ϵ is turbulence dissipation rate .

2.3. Law of wall

In the vicinity of the wall, the turbulent behaviour of flow is strongly influenced by the presence of the wall. And up to certain extant, the internal and external flow shows resemblance near the wall. The law of wall is empirically determined relationships and according to that for both internal and external flows, the streamwise velocity in the flow near to the wall varies logarithmically with the distance from the boundary [4]. Near the surface, the effect of inertial forces and pressure gradient becomes smaller. Here the effect of the rate at which momentum is transferred to the surface, per unit area per unit time, and molecular diffusion of momentum becomes larger. The momentum transfer is equal to shear stress, τ, and molecular diffusion is measured in terms of kinematic viscosity, ν.

The friction velocity is defined as

$$u_\tau = \sqrt{\frac{\tau_w}{\rho}}, \tag{2.13}$$

which is velocity scale representing the velocity close to the solid boundary. The length scale is given by ν/u_τ. Here ρ is the density and τ_w is wall shear stress defined as:

$$\tau_w = \mu\left(\frac{\partial u}{\partial y}\right)_{y=0}, \tag{2.14}$$

where u is the flow velocity parallel to the wall and μ is the dynamic viscosity and y is the distance to the wall. For the discussion of velocity profile and turbulent boundary layer the dimensionless units of velocity and distance is used, which are defined as

$$\begin{aligned} u^+ &= \frac{U}{u_\tau}, \\ y^+ &= \frac{u_\tau y}{\nu}. \end{aligned} \tag{2.15}$$

The flow near the wall is divided into different regions based on the behaviour of the flow properties. Figure 2.2 shows the schematic representation of various layers and sublayers, along with the energy production and dissipation curves for each layer.

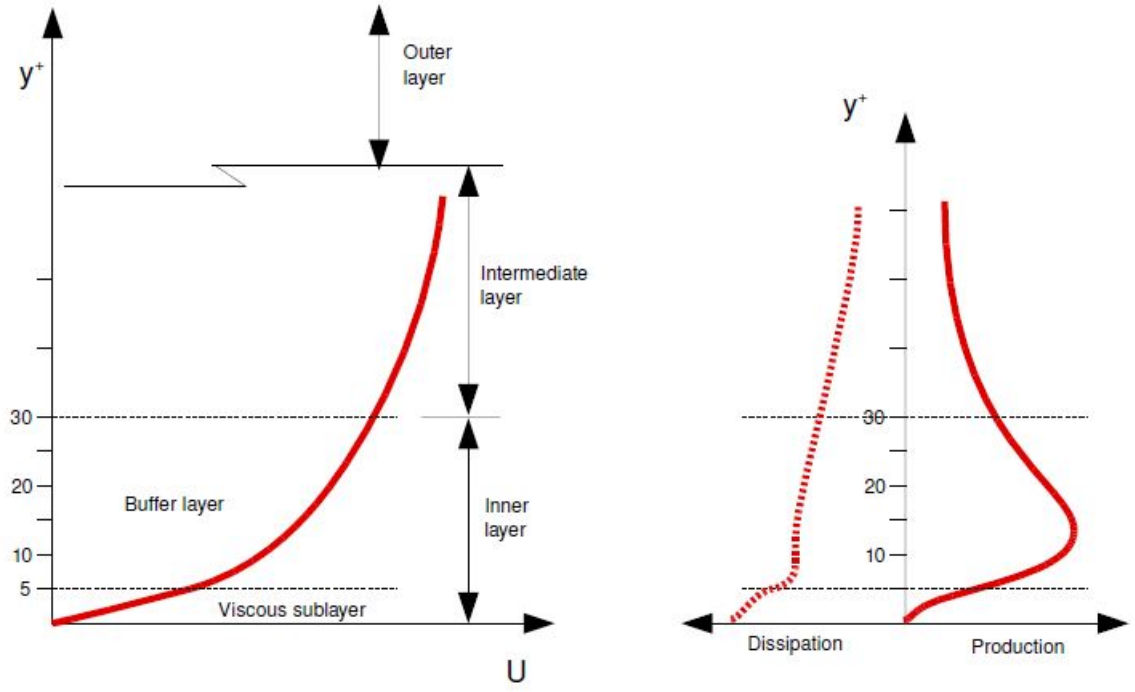

Figure 2.2: Nomenclature for wall-bounded turbulent flows(left) and respective turbulent energy production and dissipation curves(right), adopted from [4].

In the inner layer, also known as the viscous layer, viscosity has a significant effect on flow behaviour. It is sub-divided into viscous sublayer, where viscosity dominates, and the buffer layer, where both viscosity and eddies effect is pronounced. The intermediate layer also known as log layer is dominated by the inviscid turbulent phenomenon. The outer layer is also termed as defect layer in the literature.

Figure 2.3 shows the velocity profile for a turbulent boundary layer. With the representation of laws used to describe the flow in the regions.

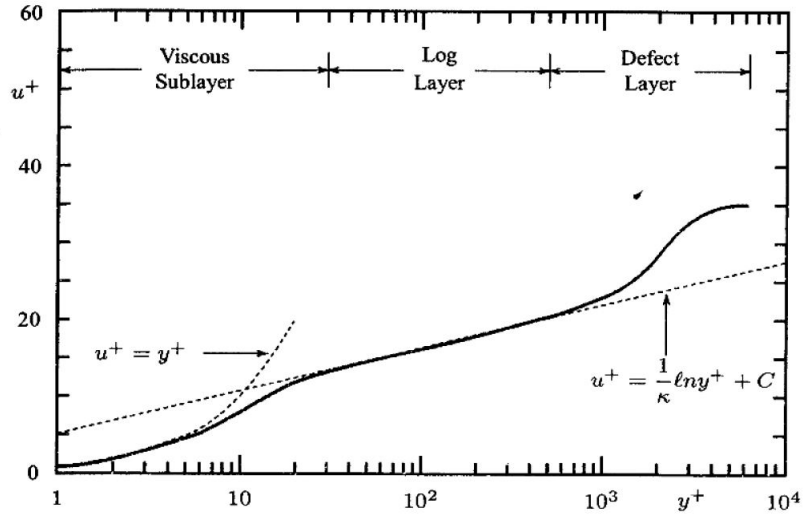

Figure 2.3: Typical velocity profile for turbulent boundary layer, adopted from [4].

In the viscous sublayer, the velocity profile the dimensionless velocity, u^+, depends on the distance as

$$u^+ = y^+, \tag{2.16}$$

which applies till the distance, y^+ of 5 in viscous layer [4]. In the intermediate layer, the log law is used to define the velocity profile :

$$u^+ = \frac{1}{k} ln y^+ + C, \tag{2.17}$$

where Karman constant, k is equal to 0.4 and C ranges from 5−5.5 and depends on roughness height.

3

Governing Equations

The behaviour of flow is governed by some principle equations that contain various elements which determine the flow physics. Based on the flow conditions and scenario of interest, different forms of these equation can be formulated using some assumptions. In this chapter, the equations and assumptions which are used in this thesis project are discussed.

3.1. Navier-Stokes equation

The laminar flows are layered, regular, smooth and ordered whereas turbulent flows disordered, fluctuating and chaotic. Both laminar and turbulent flow flow obey the same equations of motion. The Navier-Stokes equation form a system of nonlinear partial differential equations, describing the relation between the variables of flow, such as velocity and pressure, as a function of position and time [22]. The essential aspect of Newton's laws, and thus of the Navier–Stokes equations, is that they are deterministic. This means that in principle, given the equations of motion together with the initial and boundary conditions, the evolution of the flow field can be computed as a function of time; hence, the solution to the equations and conditions that describe the flow can be completely determined [22].

Here in this section only incompressible equation are mentioned with the constant density, which will be used for this thesis project. The equations are expressed in terms of material derivative of flow properties as:

Continuity equation is based on the principle of mass conservation.

And it can be expressed as:

$$\nabla \cdot \vec{u} = 0. \tag{3.1}$$

Momentum equation derived on the principle of newton's second law of motion is expressed as :

$$\rho \frac{D\vec{u}}{Dt} = -\nabla p + \rho \vec{g} + \mu \nabla^2 \vec{u}. \tag{3.2}$$

Energy equation based on conservation of energy can be written as:

$$\frac{DT}{Dt} = \alpha \nabla^2 T, \tag{3.3}$$

where, $\vec{u}$ is the velocity vector, ρ is the density, p represents the pressure, μ is the dynamic viscosity, α is the thermal diffusivity and T is the temperature.

3.2. Boussinesq approximation

In scenarios where the flow with different temperature and hence different density mixes, the assumption of incompressible fluid cannot be strictly applied to all the cases. There are the situations when the density variations are highly dependent on the pressure variations and the medium is considered compressible, such as [23]

- Steady flow with large Mach numbers. With increase in Mach no. large pressure changes produces large density changes. Until the Mach no. of 0.3 the compressibility effects can be neglected.
- Highly unsteady flow where the pressure changes and density changes are unpredictable and depend on position and time.
- As in the heterogeneous fluid, density varies with the height due to gravity. When the vertical scale of the flow is so large that the hydrostatic pressure variations causes large changes in the density.

When the compressibility effects are negligible and the change in density is a direct result of the temperature differences only, the Boussinesq approximation can be used. This approximation is applicable for the small density and temperature differences and is very suitable for the cases with water as working medium, since water is nearly incompressible. This approximation states that the density change is important only for the body forces and not in other terms. Generally, this body force is gravity and is typically important only in that directional component of the momentum equation in which the gravity is acting. The other important assumption of this approximation is that the properties of fluid, such as (μ, K, c_p, β) should be considered temperature independent and are taken at the reference temperature [23].

For the following discussion, terms with subscript, o, are the reference physical quantities which can be considered at some reference temperature. The unsteady Navier-Stokes equation with Boussinesq approximation can be shown as
Continuity equation :

$$\nabla \cdot \vec{u} = 0. \tag{3.4}$$

Momentum Equation :

$$\frac{Du}{Dt} = -\frac{1}{\rho_o}\frac{\partial p}{\partial x} + \nu\nabla^2 u, \tag{3.5}$$

$$\rho_o \frac{Dv}{Dt} = -\frac{\partial p}{\partial y} - \rho g + \mu\nabla^2 v, \tag{3.6}$$

$$\frac{Dw}{Dt} = -\frac{1}{\rho_o}\frac{\partial p}{\partial z} + \nu\nabla^2 w, \tag{3.7}$$

where gravity, g, is acting in the y-direction. Therefore, the body force term is only included in the y-momentum equation and ρ is the density which is dependent on the temperature as

$$\rho = \rho_o[1 - \beta(T - T_o)], \tag{3.8}$$

where ρ_o is the reference density corresponding to the reference temperature T_0, β is the thermal expansion coefficient and T is the temperature which will be deduced from the following energy equation.

$$\frac{DT}{Dt} = \alpha\nabla^2 T. \tag{3.9}$$

where α is the thermal diffusivity.

For the natural convection case, the y-momentum equation can be further simplified with the help of boundary layer analysis. In a boundary layer, the pressure is the function of dominant flow direction. Therefore,

$$\frac{\partial p}{\partial y} = \frac{dp_o}{dy}. \tag{3.10}$$

In the natural convection scenario, the u at the edge of the boundary layer will be 0 as there is no external mechanism to derive the bulk flow. Therefore dP_o/dy will be defined by hydrostatic pressure gradient as

$$\frac{dp_o}{dy} = -\rho_o g. \tag{3.11}$$

Now, using Equations (3.8) and (3.11), (3.12) can be written in a simplified form without pressure gradient and density terms as

$$\frac{Dv}{Dt} = g\beta(T - T_o) + \nu\nabla^2 v, \tag{3.12}$$

3.3. Governing equations for Rayleigh Bénard convection (RBC) study

The governing equations which will be used for the validation study, given in Chapter 7, are discussed here. This equations and method of non-dimensionalising the equation in terms of Rayleigh number and Prandtl number was used by Kooij et al. [10] and Roberto et al. [9].

3.3.1. Rayleigh number

Rayleigh number, Ra, represents the ratio of the destabilising effect of buoyancy force to the stabilising effect of viscous force. When the layer of fluid is heated from below, the temperature of fluid at the bottom will rise resulting in relatively lower density and therefore have a tendency to move up. Due to the viscosity and thermal diffusivity, the convection motion of fluid will not occur. Only at a sufficiently large thermal gradient the layer becomes unstable. With the help of a non-dimensional number, Ra, this can be characterised. In essence, above certain value of Ra* (critical Ra), the instability will occur. The Rayleigh number is expressed as

$$Ra = \frac{g\beta\Delta T H^3}{\nu\alpha}, \tag{3.13}$$

where g is the accelaration due to gravity, β is the thermal expansion coefficient, ΔT is the temperature difference between the plates, H is the distance between top and bottom of the layer, ν is the kinematic viscosity, and α is the thermal diffusivity expressed as

$$\alpha = \frac{K}{\rho c_p}, \tag{3.14}$$

where K is the thermal conductivity, ρ is the density and c_p is the specific heat capacity.

3.3.2. Prandtl number

Prandtl number, Pr, is non-dimensional parameter which is ratio of momentum to thermal diffusion. And is expressed as:

$$Pr = \frac{\mu c_p}{\alpha}, \tag{3.15}$$

where μ is the dynamic viscosity, c_p is the specific heat capacity and α is the thermal diffusivity.

For the numerical simulation of Rayleigh Bénard convection, the governing Navier-Stokes equation has to be non-dimensionalised to help in generalising the flow scenario on Ra instead of individual parameters. The governing equations are non-dimensionalised based on the free-fall velocity, $U = \sqrt{g\beta\Delta T H}$ [24]. The actual quantities are represented with usual respective symbols and the non-dimensionalised parameters are represented with a star (*) symbol. This convention will be followed for the rest of this section. Using this, the rest of the terms can be non-dimensionalised as follows

Time:

$$t = \frac{H}{U}t^* = \frac{H}{\sqrt{g\beta\Delta T H}}t^*. \tag{3.16}$$

Directional vectors:

$$(x, y, z) = (Hx^*, Hy^*, Hz^*). \tag{3.17}$$

Pressure:

$$p = U^2\rho_o p^* = g\beta\Delta T H\rho_o p^*. \tag{3.18}$$

Temperature:

$$T = \Delta T T^* + T_o. \tag{3.19}$$

The non-dimensionalised unsteady Navier-Stokes equations with Boussinesq approximation used for RBC validation study, discussed in the Chapter 7, are

$$\nabla \cdot \vec{u} = 0, \tag{3.20}$$

$$\frac{D\vec{u}}{Dt} = -\nabla p + T\hat{k} + \left(\frac{Pr}{Ra}\right)^{1/2} \nabla^2 \vec{u}, \tag{3.21}$$

$$\frac{DT}{Dt} = \frac{1}{(PrRa)^{1/2}} \nabla^2 T, \tag{3.22}$$

where $\vec{u}$ is the velocity vector, p represents the pressure, Pr is the Prandtl number, Ra is the Rayleigh number, $\hat{k}$ is the versor of the gravity force and T is the temperature.

4

Numerical Methodology

This chapter will discuss the different numerical methodologies which are used for the numerical simulations of pressurised thermal shock (PTS) scenario (discussed in Chapter 6) and validation study of Rayleigh Bénard convection (discussed in Chapter 7).

4.1. Reynolds-averaged Navier-Stokes (RANS) equation

Time averaging continuity and momentum equation gives the Reynolds averaged equations of motion:

$$\frac{\partial U_i}{\partial x_i} = 0, \tag{4.1}$$

$$\rho\frac{\partial U_i}{\partial t} + \rho U_j\frac{\partial U_i}{\partial x_j} = -\frac{\partial P}{\partial x_i} + \frac{\partial}{\partial x_j}(2\mu S_{ji} - \rho\overline{u_j' u_i'}). \tag{4.2}$$

Equation (4.2) is usually referred as the Reynolds-averaged Navier-Stokes (RANS) equation. The difference between time-averaged and instantaneous momentum equations is the presence of the correlation $\overline{u_j' u_i'}$. This term shows the time-averaged rate of momentum transfer due to the turbulence [4].

The fundamental problem of turbulence studies is to find a way to determine $\overline{u_j' u_i'}$. The quantity $-\overline{u_j' u_i'}$ is called Reynolds-stress tensor and is expressed as:

$$\tau_{ij} = -\overline{u_j' u_i'}. \tag{4.3}$$

This tensor has six components and along with the 4 flow variables, i.e. pressure and three velocity components, in total there will be 10 unknowns to be determined with the help of 4 equations. Therefore, the system is not closed and requirement of extra equations to determine the stress tensor components arises.

4.2. Standard k-ϵ turbulence model

The $k-\epsilon$ model given by Jones and Launder [25] assumes an equilibrium of turbulence production and dissipation. Isotropic turbulence follows a linear relation between Reynolds stress and shear stress as follows:

$$\mu_T = \rho C_\mu k^2/\epsilon, \tag{4.4}$$

where μ_T is a proportionality factor called eddy viscosity, which is used to relate the Reynolds stress tensor (τ_{ij}) with mean shear rate (S_{ij}) (for further detail see Section A.6). The turbulent kinetic energy (k) will be solved from the equation

$$\rho\frac{\partial k}{\partial t} + \rho U_j\frac{\partial k}{\partial x_j} = \tau_{ij}\frac{\partial U_i}{\partial x_j} - \rho\epsilon + \frac{\partial}{\partial x_j}\left[(\mu + \mu_T/\sigma_k)\frac{\partial k}{\partial x_j}\right]. \tag{4.5}$$

For further detail of the process of reaching to this equation of turbulent kinetic energy, see Section A.7. Although there is an exact transport equation for dissipation but due to its complexity the dissipation equation is postulated similar to the turbulence kinetic energy equation. The dissipation rate, ϵ, will be solved from the equation below.

$$\rho\frac{\partial \epsilon}{\partial t} + \rho U_j \frac{\partial \epsilon}{\partial x_j} = C_{\epsilon 1}\frac{\epsilon}{k}\tau_{ij}\frac{\partial U_i}{\partial x_j} - C_{\epsilon 2}\rho\frac{\epsilon^2}{k} + \frac{\partial}{\partial x_j}\Big[(\mu + \mu_T/\sigma_\epsilon)\frac{\partial \epsilon}{\partial x_j}\Big]. \tag{4.6}$$

Closure Coefficients

$C_{\epsilon 1} = 1.44$, $C_{\epsilon 2} = 1.92$, $C_\mu = 0.09$, $\sigma_k = 1.0$, $\sigma_\epsilon = 1.3$

There are different model variants and parameter set. The one above corresponds to the standard $k-\epsilon$ model.

This turbulence model provides good results for external flows, but has limitations with strong pressure gradients and separation of flow. As this model is based on eddy viscosity hypothesis, it can't distinguish between the effects of individual components of the Reynolds stress tensor. And the assumption of isotropic turbulence and energy equilibrium doesn't hold in boundary layers. But due to its comparative simplicity and low requirement of computational overhead it is one of the most used turbulence model in industrial application.

4.3. Direct numerical simulation

Direct numerical simulation (DNS) refers to the solving the Navier-Stokes equation without any turbulence modelling whatsoever. Theoretically, the time-dependent Navier-Stokes equation sufficiently contains the physics of the turbulent flow. As quoted by Tennekes and Lumley [26], " Even the smallest scales occurring in a turbulent flow are ordinarily far larger than any molecular length scale". Therefore, DNS is capable to resolves all the relevant scales of the motion. Although it is difficult yet possible to resolve the scales of turbulence motion. A lot of emphasis is put on finding the most advanced way, like discretization with high accuracy, efficient time marching schemes, effective parallel computing and accurate numerical solver to facilitate the DNS.

A three-dimensional DNS can provide detailed information about the flow physics and flow properties, like vorticity, three-dimensional velocity fields, which cannot be measured using experiments. Thereby, it can help in making a complete database of the case. Furthermore, the results of the DNS are used for the verification and validation of the turbulence models, to observe some characteristic behaviour for developing some new theories, and validating the results of computing techniques like RANS and LES.

However, the limitation of DNS in terms of computation time and costs restricts its usability for the study of all the flow scenarios. It is only possible to perform DNS for the flow with Reynolds number in the range of low thousands. The flow resolution and number of time steps required for the simulation both depends on Kolmogorov and Batchelor length scales. As discussed earlier, the size of smallest scales reduces exponentially with increase in Reynolds number. For the accurate numerical simulation (i.e., a full time-dependent three-dimensional solution) of a turbulent flow, all physically relevant scales must be resolved [4]. This leads to higher computational overhead which roughly scales with $(Re)^3$. To limit the number of elements and thereby the cost of DNS, normally a portion of physical domain is simulated after simplifying the domain and flow parameters. Generally, for homogeneous flows, periodic boundary conditions are applied by keeping the boundaries far enough so that the correlations between their local turbulence dynamics and those of the rest of the flow are assumed to be not significant. And the reasons and limitation mentioned here, will govern the PTS numerical case's design process.

4.4. Spatial discretization

The solver which will be used for the PTS and RBC simulations are Star-ccm+ and NEK5000 which are based on finite volume method and spectral element method respectively. In this section a brief background of the two methods is discussed.

4.4.1. Finite volume method

The finite volume method uses the integral form of conservation equation as the starting point. The transport equation for the scalar quantity, ϕ, is used for the discussion :

$$\frac{\partial}{\partial t}\int_V \rho\phi dV + \int_S \rho\phi v.ndS = \int_S \Gamma\nabla\phi.ndS + \int_V q_\phi dV, \tag{4.7}$$

where Γ shows the diffusivity of ϕ and q_ϕ is the source or sink term of ϕ.
In the above equation the terms appearing are, moving from left to right, transient, convective flux, diffusive flux and volumetric source or sink term.

In this method, the solution domain is divided into a finite number of smaller domains called control volumes (CV) by means of grids which marks the CV boundaries. In every CV the conservation equations are applied. At the centre of each CV a computational node is defined at which the variable's value is calculated. By interpolation the variable's values at the surface of CV is calculated. The surface and volume integrals are approximated by suitable quadrature formulae [5].

For the simplicity of discussion the equation here are discussed for the 2D Cartesian grid and Figure 4.1 shows the schematic representation and nomenclature which is followed in the discussion.

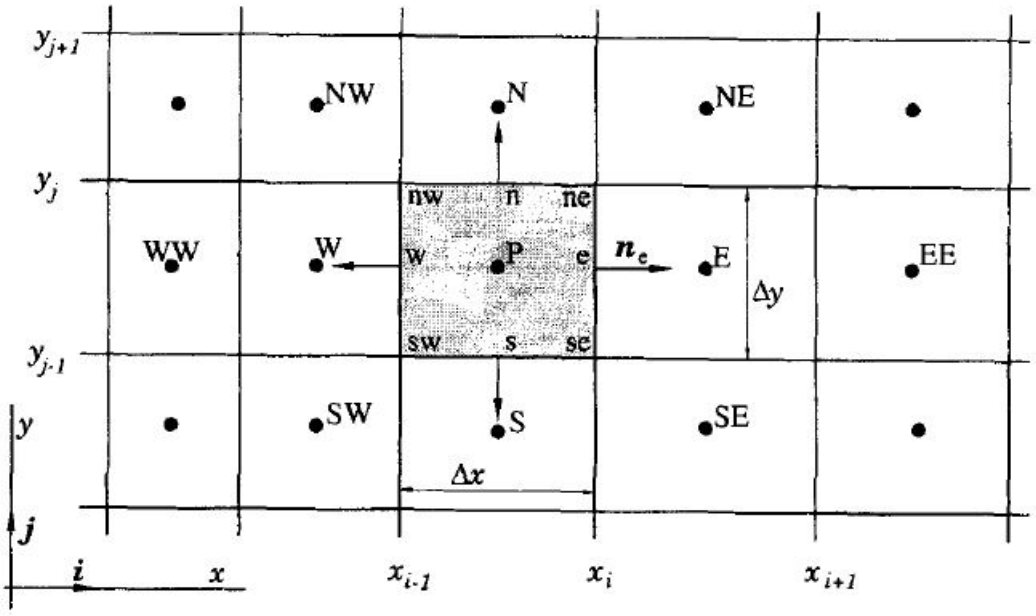

Figure 4.1: Control volume representation with notation for a 2D grid, adopted from [5].

The following sections will discuss the ways and methods generally used for the approximation of the surface and volume integral also the interpolation methods.

Approximation of surface integrals

The net flux through the CV boundaries is calculated by the summation of integrals over the CV faces, which can be expressed in the form as

$$\int_S f dS = \sum_k \int_{S_k} f dS. \tag{4.8}$$

Here, f is the component of the convective ($\rho\phi v.n$) or diffusive ($T\Gamma\nabla\phi.n$) flux vector in the direction normal to CV face. For the following discussion, the CV face labelled as 'e' is taken as reference. The expression for other faces can be calculated in similar fashion.

As only the variable's value at node (CV center) is known. Firstly for the surface integral, the integral value is approximated by means of values at one or more locations on the cell face. And the cell face

value is approximated in terms of nodal values. The approximation for the integral can be done using: Mid-point rule (second order approximation), which is most commonly used by taking product of f at cente of 'e' and surface area of face 'e'.

$$F_e = \int_{S_e} f dS = \overline{f_e} S_e \approx f_e S_e. \tag{4.9}$$

Trapezoidal rule (second order approximation)

$$F_e = \int_{S_e} f dS \approx \frac{S_e}{2}(f_{ne} + f_{se}). \tag{4.10}$$

Simpson rule (fourth order approximation):

$$F_e = \int_{S_e} f dS \approx \frac{S_e}{6}(f_{ne} + 4f_e + f_{se}). \tag{4.11}$$

Since the value at point on face surface of 'e' is not known it has to be interpolated from the value at the nodes, which is discussed later. Another important consideration which has to be taken is that for the second order approximation, at least second order interpolation scheme should be chosen.

Approximation of volume integral

i 8 The simplest second-order accurate method of approximating the volume integral is done by replacing the integral with the product of mean value of integrand and volume of the CV. The mean value of integrand is approximated by the value at node (CV centre).

$$Q_p = \int_V q dV = \overline{q} \Delta V \approx q_p \Delta V. \tag{4.12}$$

Since all variables value are known at the node, interpolation is not required.

Interpolation and differentiation Practices

Upwind difference scheme

As discussed earlier, for the calculation of convective and diffusive part (surface integrals) nodal values are used for the interpolation. The upwind differencing scheme (UDS), is similar to employing BDS (backward differencing scheme) or FDS (forward differencing scheme). As it assigns the value of ϕ_e as that of the upstream or downstream node depending on the flow direction, as expressed in the equation below. Based on the number of nodes point used for the interpolation determines the order of the upwind scheme. Generally second order upwind scheme is used for numerical simulations.

$$\phi_e = \begin{cases} \phi_P & \text{if } (v.n)_e > 0 \\ \phi_E & \text{if } (v.n)_e < 0\ . \end{cases} \tag{4.13}$$

The method of finite volume is more suitable forwd complex geometries. One of the disadvantages of FV method is the difficulty in developing higher than second order method in 3D because of three levels of approximation : interpolation, differentiation, and integration [5].

4.4.2. Spectral element method

The spectral element method (SEM) is an advanced method that has the attributes of both finite element and spectral method. In finite element method (FEM), the domain is divided into small non-overlapping domains and the solution of actual function is approximated with the help of local functions (whose value becomes zero outside of these domains) whereas in spectral method the solution is approximated using combination of global functions which are extended on the overall domain. The SEM is basically FEM with higher order orthogonal polynomials. [27]. The following sections will discuss briefly the spectral element method and how it is related FEM and spectral method.

Spectral discretization

In spectral methods and FEM, the approximate solution of the function is found by means of finite number of functions as

$$u(x) \approx u_N(x) = \sum_{i}^{N} q_i \phi_i(x), \tag{4.14}$$

where $\phi_i(x)$ are the basis functions and q_i is the unknown weights. The difference between the two methods is that the former uses a finite number of global functions whereas FEM uses finite number of local functions. The basis functions are generally Chebyshev polynomials or Legendre polynomials. Spectral methods are classified into collocations and Galerkin methods. Galerkin method is a special case of weighted residual method (WRM) .

Weighted residual method

As we are approximating the exact solution by replacing the infinite expansion to a finite one, the differential equations can't be satisfied in the whole domain rather it will satisfy only at fixed number of conditions. If we consider linear differential equation dependent on a quantity 'u' as

$$L(u) = 0, \tag{4.15}$$

which has defined initial and boundary conditions. The solution $u(x,t)$ can be approximated by solution of the form :

$$u^{\delta}(x,t) = u_0(x,t) + \sum_{i=1}^{N_{dof}} \hat{u}_i(t)\Phi(x), \tag{4.16}$$

where $\Phi_i(x)$ are the trial (or expansion) functions, $\hat{u}_i(t)$ and the N_{dof} unknown coefficients and $u_o(x,t)$ will satisfy the initial and boundary conditions.

Using the above mentioned approximate solution 'u^{δ}' for soving the differential equation will produce some non-zero residual,R such that

$$L(u^{\delta}) = R(u^{\delta}). \tag{4.17}$$

To determine the unknown coefficient $\hat{u}_i(t)$, condition on residual is imposed which result in system of ordinary differential equations in terms of $\hat{u}_i(t)$ as :

$$(v_j(x), R) = \int_{\Omega} v_j(x) R dx = 0 \quad j = 1, ..., N_{dof}, \tag{4.18}$$

Here, the expression $(v_j(x),R)$ denotes the inner product of residual to weight function (or test function), $v_j(x)$. The inner product is a scalar quantity that provides the measure of similarity between two function, therefore 0 corresponds to orthogonal functions. The residual will tend to zero on convergence as the approximate solution, $u^{\delta}(x,t)$, approaches the exact solution, $u(x,t)$, when $N_{dof} \rightarrow \infty$. Choice of appropriate expansion (trial) and test function is important. The most used scheme for selecting the test function is based on the Galerkin method. Where the test function (v_j) is chosen to be same as trial function Φ_i. The expansion function used for spectral method has to be smooth in the whole domain and for finite element method uses a set of expansion function for the local finite region [27].

For both spectral and FEM, polynomial expansions are used. To get a convergence of solution there are two ways viz., h-type and p-type method. The spectral element method combines the attributes of both discretization methods i.e, h-type (element size) and p-type method (polynomial order).

h-type method

In the h-type method, the order of the polynomial is fixed for every element and by means of increasing the number of elements, the convergence is achieved. This is called h-type extension process. Here h represents the characteristic size of the element. In this method, the solution domain is divided into sub-domains which are non-overlapping and the polynomial expansions are solved locally within these elements, which increases the efficiency of the operation and simplifies the implementation. By refining the mesh, i.e, increasing the number of elements while keeping the order of polynomial same the error decays [27].

p-type expansions

In the p-type method polynomial expansions of higher order are selected. Here p represents the order of the polynomial. When this polynomial expansions are used in a single domain it comes under the framework of spectral methods. However, it is difficult to find the global expansion analytically. These high order polynomials can be decomposed in the elemental domain as well. The choice of elemental polynomial expansions depends upon its feasibility and ease with which it can be numerically implemented. Orthogonal or near orthogonal set of functions are used as expansion functions.

In contrast to the h-type method, the convergence can be achieved by increasing the order of the polynomial expansions while keeping the size of sub-domains constant which will reduce the error in numerical solution. This technique is called p-enrichment and it is capable of exponential decay of numerical error when the solution is smooth.

Polynomial nodal expansions

Lagrange polynomials of order p is based on a set of p+1 nodal points, x_q. These nodal points, referred to as nodes, play an important role in determining the polynomial shape and characteristic. When Lagrange polynomials are used as expansion basis, they are referred as polynomial nodal expansion. In the nodal expansion, an approximate solution doesn't necessarily satisfy the equation exactly at nodes [27].

The selection of nodal points has a restriction on including the ends of the domain whether it be the end of sub-domains in case of FEM or end of the global domain in case of spectral method. Rest of nodal points can be selected at any location in the interior domain. But the selections of these nodes has an effect on the stability of the approximation and conditioning of the system [27]. One of the locations of the commonly used nodes are the zeros of the Gauss-Legendre-Lobatto (GLL) integration rule resulting in expansions which do not exhibit oscillations in the solutions. A comparison of Lagrange polynomial through equi-spaced nodal point and through GLL points is shown in Figure 4.2. It can be observed that the polynomial behaviour becomes oscillatory for N $\geq$ 7, N represents the order of the polynomial, and even result in negative quadrature weights for N $\geq$ 8 on the other hand GLL distribution is a stable formulation.

In a Spectral element method, Lagrange polynomials through the Gauss-Legendre-Lobatto (GLL) points form the expansion basis. These GLL points form a grid which can be seen as a sub-element within the super element (h-type) and in this way it has the attributes of FEM. Global accuracy can be achieved by both the refinement of super elements and increasing the order of the polynomial. The Figure 4.3 shows a schematic representation of GLL point distribution for different value of the polynomial order. With increasing the order, more number of nodes will be required to approximation the polynomial, leading to better approximation.

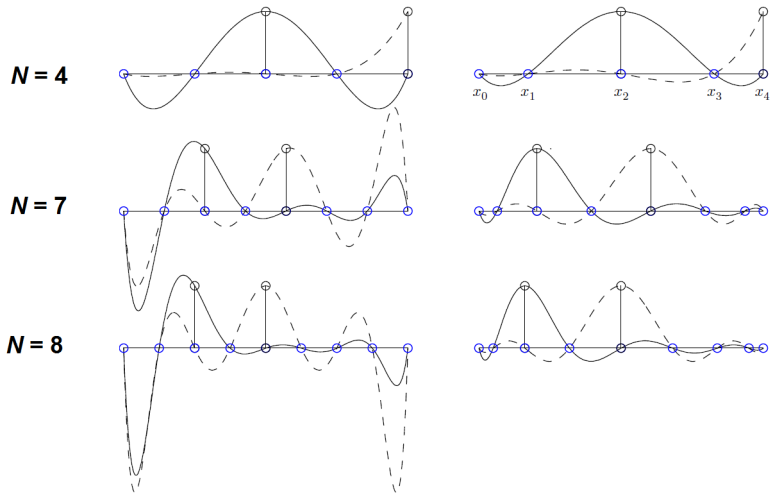

Figure 4.2: Two Lagrange Polynomials based on equi-spaced (left) and GLL points distribution (right), adopted from [6].

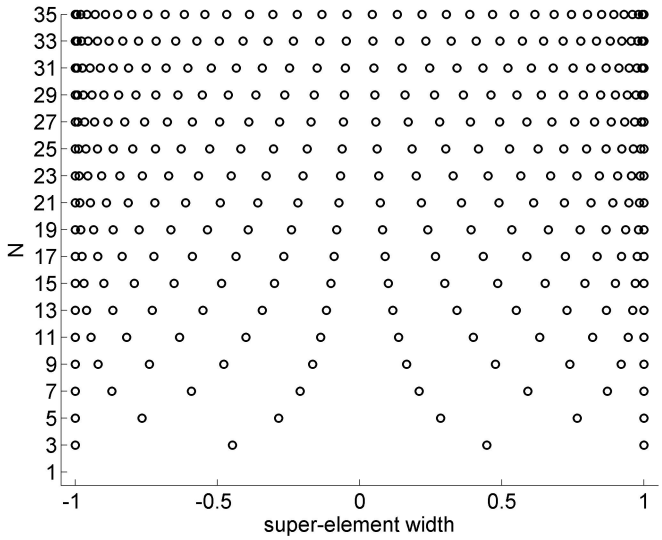

Figure 4.3: Gauss-Lobatto-Legendre (GLL) points distribution along a single direction inside a super-element for different polynomial order N, adopted form [7].

4.5. Time marching method

For the unsteady flow scenarios where the flow behaviour is dependent on time, the discretization of the 4th dimension, time, is required. There are two basic time marching methods viz. implicit and explicit. Based on the selection of the grid point and time steps used, these methods are sub categorised. The time discretization is done using same methods as spatial discretization. But, the main difference between the space and time marching is that in the former, a force at any space location may influence the flow in other locations but in later one, forcing will effect only in the future time, so no backward influence. The following section will discuss about the explicit and implicit methods. In the following equations the time step is represented by 'n', spatial step by 'i', ϕ is the unknown quantity and Δt is the time step size.

4.5.1. Explicit method

In the explicit method, the unknown quantity at next time step will be deduced from the known quantities of previous time step(s). Therefore, this method is straightforward and easier to implement as compared to the implicit method.

Forward Euler rule (first order accuracy):

$$\phi^{n+1} = \phi^n + f(t_n, \phi^n)\Delta t. \tag{4.19}$$

For the fixed spatial size (Δx), based on the stability criterion the time step size is decided. And generally, time step size is very small to maintain and result in larger computational time.

4.5.2. Implicit method

In implicit methods, the difference equation will be solved simultaneously for all the grid points at same time level to deduce the unknown. This simultaneous equation solution requires large matrix manipulations and therefore requires large computational time for each time step.

There are three generally used rules in implicit method, Euler backward, mid-point and trapezoidal rule.

Euler backward (first order accuracy) :

$$\phi^{n+1} = \phi^n + f(t_{n+1}, \phi^{n+1})\Delta t. \tag{4.20}$$

Here, the unknown at next time step will be deduced by the known quantity at the current time step and the

Mid-Point rule (second order accuracy):

$$\phi^{n+1} = \phi^n + f(t_{n+1/2}, \phi^{n+1/2})\Delta t. \tag{4.21}$$

Trapezoidal Rule (second order accuracy):

$$\phi^{n+1} = \phi^n + \frac{f(t_n, \phi^n) + f(t_{n+1}, \phi^{n+1})}{2}\Delta t. \tag{4.22}$$

Second order implicit method:

As the first order backward Euler is not too accurate and because of its first order truncation error in time, it requires lot of coupled set of equations at each time step. Instead, second order implicit scheme can be used, which require the information of three time steps instead of two. It takes into account the additional information from one time step lower than current time step to determine the next time step, as expressed in equation below:

$$\phi^{n+1} = \frac{4}{3}\phi^n - \frac{1}{3}\phi^{n-1} + \frac{2}{3}f(t_{n+1}, \phi^{n+1})\Delta t \tag{4.23}$$

The implicit methods are more stable for the same Δt corresponding to explicit methods. As the stability can be achieved for a larger time step, fewer time steps will be required for same physical time simulation. Due to large matrix manipulations for simultaneous solution of the equations, the computation time will be larger for each time step.

4.5.3. Implicit/Explicit Method (IMEX)

In Nek5000, for symmetric and linear terms implicit method is used whereas the nonlinear, non-symmetric and the user provided, including Boussinesq and Coriolis forcing, terms are solved using explicit method. Solving all the terms implicitly is computationally demanding and for the stability reasons some terms are solved explicitly. In this section, the method used in Nek5000 and the way of approach is discussed in brief.

Consider the generalised time dependent problem, subjected to initial condition given by u_0, which can be written in the form

$$\frac{\partial u}{\partial t} = S[u], \qquad u(t_0, x) = u_0 \tag{4.24}$$

where the spatial operators are represented as S[·].

In this discussion a general formulation of time marching is discussed for k^{th} order. The order of method, k, can be ≤ 3. The k^{th} order backward differencing formula to approximate the time derivative $\partial u/\partial t$ is given as

$$\sum_{j=0}^{k} b_j u^{(n+1-j)} = \Delta t S[u^{n+1}], \tag{4.25}$$

The k^{th} order extrapolation formula is given as

$$S[u^{n+1}] = \sum_{j=1}^{k} a_j S[u^{n+1-j}], \tag{4.26}$$

The value of the above-mentioned coefficients a_j an b_j are given in the Tables 4.1 and 4.2. Depending on the order of method used for the interpolation or extrapolation the coefficient's values will be used.

	EXTk		
k	a_1	a_2	a_3
1	1		
2	2	-1	
3	3	-3	1

Table 4.1: Coefficients for the k-th order extrapolation (EXTk) schemes with k ≤ 3. For a given k, the coefficients are a_j with 1 ≤ j ≤ k. Adopted from [6].

	BDFk			
k	b_0	b_1	b_2	b_3
1	1	-1		
2	$\frac{3}{2}$	$-\frac{4}{2}$	$\frac{1}{2}$	
3	$\frac{11}{6}$	$-\frac{18}{6}$	$\frac{9}{6}$	$-\frac{2}{6}$

Table 4.2: Coefficients for the k-step backward-difference (BDFk) schemes with k ≤ 3. For a given k, the coefficients are b_j with 0 ≤ j ≤ k. Adopted from [6].

For brevity of the explanation, the time discretisation by implicit/explicit scheme (IMEX) is explained here in terms of Convection-Diffusion equation. A SEM discretised higher order passive scalar given by Convection-Diffusion equation as

$$M\frac{du}{dt} = Au - Cu + Mf, \tag{4.27}$$

where M represents a diagonal matrix and holds the weights of the the quadrature rule at the diagonals. C is the convective operator and A represents the stiffness matrix corresponding to the second order term (Laplacian).

If we solve the Equation (4.27) by Implicit/Explicit method, i.e. by using backward differencing (BDF) and extrapolation (EXT) for the explicit step, the equation can be expressed as

$$\sum_{j=0}^{k} \frac{b_j}{\Delta t} M u^{n+1-j} = Au^{n+1} - \sum_{j=1}^{k} a_j C u^{n+1-j} + Mf^{n+1}. \tag{4.28}$$

Here the time derivative part is implicitly solved with backward differencing of k^{th} order and convective term, Cu, is extrapolated with k^{th} order. On rearranging the equation will take a form ,

$$(\frac{b_0}{\Delta t}M - A)u^{n+1} = -\sum_{j=1}^{k} a_j C u^{n+1-j} - \sum_{j=1}^{k} \frac{b_j}{\Delta t} M u^{n+1-j} + Mf^{n+1} \tag{4.29}$$

This system of equations will be solved by summing up the last terms of the RHS, the lagged BDF and the forcing, and later the extrapolated convective term is added resulting in the complete RHS.

5

PTS study - without buoyancy effects

The research program at NRG for PTS studies, discussed in detail in Section 1.6, started with numerical study of PTS scenario without buoyancy effects. In the current thesis project, the study is performed on the PTS scenario with buoyancy effects which is a continuation of the previous work. Therefore, a summary of the final conclusions and considerations of the past work performed without considering buoyancy effects are given in this chapter, before moving to the discussion of study performed in this thesis project. In Section 5.1, the past numerical study of Shams et al. [8] on PTS without buoyancy effects is discussed and finally motivation and requirement of PTS study with buoyancy effect is given in Section 5.2.

5.1. Shams et al. study on PTS without buoyancy effects.

Owing to the limitations of DNS, a very simple physical domain with feasible boundary conditions had to be designed. At the same time, it should have all the important attributes of actual flow scenario. Shams et al. [8] had performed a comprehensive study without considering buoyancy effects. For the numerical study of single-phase PTS without buoyancy effect, a well-defined physical domain, boundary conditions and flow conditions were achieved. The following sections will discuss the starting physical domain, the code used, simulation specifications and final flow properties, geometry and boundary conditions. Several comparative studies had been performed using RANS simulations to calibrate and optimise the selected PTS geometry.

5.1.1. Physical Domain

The computational domain represents the simplified reactor pressure vessel (RPV) with cold leg, downcomer, RPV wall and barrel (shroud) wall. Only a portion of downcomer is considered for the physical domain. The most important region is the T-junction where cold water enters into the downcomer. Due to computational limitation, the complex curve geometry or RPV is replaced with a planar configuration. Also, the lower plenum of RPV is not considered. Nek5000 is considered for the final DNS and it requires conformal and hexahedral mesh. This had a significant influence on the design of physical domain. A secondary inlet is considered at the top of the domain, to generate a downward flow path for the cold incoming water in the downcomer as no buoyancy effects are considered. The initial flow configuration is selected based on ROCOM test facility. The Figure 5.1 represents the physical domain of PTS design. And the Table 5.1 discuss the various geometrical parameters and the consideration made during the selection of them.

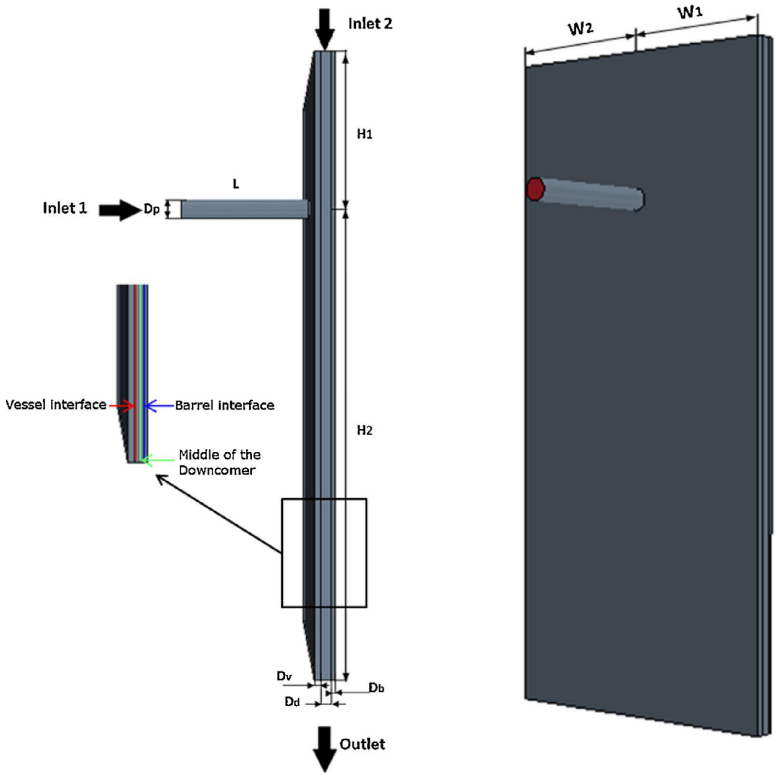

Figure 5.1: Physical domain of PTS Design, adopted from [8].

Parameter	Description	Considerations
Inlet-1	Cold water inlet	Inlet for the ECC (relatively cold) water injection.
Inlet-2	Hot downcomer water inlet	In actual scenario, such an inlet is not present. However, to force the impinging cold jet downward in the downcomer, a secondary inlet's was considered. This inlet helped in obtaining a certain level of thermal mixing between the cold leg water and the hot downcomer water as the buoyancy effect in this case was not considered.
D_p	Diameter of the cold Leg	Same as ROCOM facility's experimental setup.
L	Cold leg length	Distance from ECC injection and the downcomer inlet of the ROCOM facility.
H_1	Upper height	Height for the development of the flow from Inlet 2. The initial design value was considered the same as the cold leg (L).
H_2	Downcomer height	The initial height of $23.3D_p$ was considered, which was good enough to prevent possible reverse flow effects at the outlet. But, this height was calibrated based on the required length for development of flow fields.
W_1, W_2	Half width of the geometry	The initial width was considered same as the cold leg (L).
D_d	Thickness of the downcomer	Same as ROCOM test Facility Setup.
D_v	Thickness of the RPV wall	A 1:5 scale of an actual reactor vessel design.
D_b	Thickness of the core barrel wall	A 1:5 scale of an actual reactor vessel design.

Table 5.1: PTS Design geometric parameter and their description, adopted from [8]

Parameter	Non-dimensionalised By D_p
D_p	1
L	7
H_1	7
H_2	23.3
W_1	7
W_2	7
D_v	0.33
D_p	0.48
D_b	0.16

Table 5.2: Geometric Dimensions of the selected PTS design, adopted from [8]

The geometric dimensions of each parameter is given in Table 5.2. For simplicity and greater understanding of the dimensions of the parameters, they were non-dimensionalised by the cold leg diameter (D_p= 0.15 m, adopted from the ROCOM facility) as x^*= x/Dp.

5.1.2. Boundary conditions

For the Inlet-1 (see Figure 6.1), bulk velocity of 0.018m/s was used based on the experimental setup of ROCOM test facility, [2]. A fully developed turbulent velocity profile was imposed to sustain the turbulence level in the cold leg. The velocity at Inlet-2 (see Figure 6.1) had to be minimal because it's an artificial inlet, velocity was imposed in the percentage of Inlet-1's velocity. As the Inlet-1 represents the cold injection of water temperature of 293K was considered at this inlet. Inlet-2 forms a hot inlet as it will be at the temperature of downcomer's hot water, therefore the temperature of 353K was considered. No-slip wall boundary condition was used at all the walls. Moreover, adiabatic boundary conditions on spanwise wall and conjugate heat transfer was considered at RPV wall and shroud wall interface.

5.1.3. Flow properties

The reference properties for water was selected based on the least Prandtl number (Pr) to reduce the mesh requirement for the DNS. With reference temperature (T_o) of 293K, the Pr was of approximately 7. By increasing the temperature to 353K, the Pr decreased to 2.23. Prandtl number shows the ratio of viscous diffusion to thermal diffusion. As it is important for DNS to resolve both the smallest temperature and velocity length scales, the Prandtl number helps in determining the mesh requirement for the DNS. Higher Pr corresponds to requirement of more refinement for the temperature than for velocity. Therefore, finally temperature of 353K was used as reference temperature and the flow properties are taken to corresponding to it and the standard solid properties were taken at 323K, given in the Table 5.3.

Reference temperature T_o [K]	**Density -** ρ $[Kg/m^3]$	**Specific heat** c_p [J/(Kg.K)]	**Dynamic viscosity** μ [Pa.s]	**Thermal conductivity** K [W/(m.k)]	**Thermal expansion coeff.** α [1/K]	**Prandtl number** Pr [-]
Water 353	971.79	4196.8	3.543e-4	0.670	6.4e-4	2.23
16MND Steel 323	7840	476.50	-	45.98	-	-

Table 5.3: Material properties.

5.1.4. Final conclusions of PTS without buoyancy effects study.

These are the final results of several calibration processes which were performed for physical domain and boundary conditions:

- As the DNS was planned to performed using Nek500, which requires structured and conformal meshes. Foreseeing the limitation of Nek5000 with circular mesh, the cold leg geometry was

changed to square duct. The use of square duct in cold leg with the same hydraulic diameter, as of the circular pipe, and bulk velocity was suggested.

- The velocity at Inlet-2 (see Figure 6.1) cannot be considered too high from mesh requirement point of view. However, a reasonable flow velocity is required to push the incoming cold flow in the downcomer. Velocity of 10% of velocity at Inlet-1 was found to be a good balance between the computational requirement and the closeness of flow behaviour to the actual PTS scenario.
- As the initial geometry was just a starting point for the study, it was calibrated according to flow behaviour and effect of boundary conditions on the flow. It was found that the height of upper section of downcomer had to be increased (to $H_1 = 10D_p$) for the complete development of temperature field in upper part of the downcomer. The original height of downcomer was suggested to be optimum. Similar calibration process on the width of downcomer concluded an increase in width, $W_1 + W_2$ to $\approx 20D_p$.
- The overall computational cost of DNS is a factor of Reynolds number and roughly corresponds to Re^3. Therefore, Reynolds number scaling was considered. Two friction Reynolds number, $Re_\tau = (u_\tau D_h)/\nu$ based on mean u_τ and hydraulic diameter D_h, of 230 and 180 in the inlet duct was compared. For the DNS scaled Re_τ of 180 was finalised.

5.2. Future work prospects

During the real scenario of PTS events, the injected cold ECC water mixes with the hot water already present in the cold leg and the mixture flows downward in the downcomer in the form of buoyancy-driven thermal plumes [19]. Study of flow mixing, formation and time evolution of the thermal plumes in the downcomer is the interest of PTS study. As the study performed by Shams et al. did not considered buoyancy effects in the flow. A requirement of more detailed study on the buoyancy-driven flow in single-phase PTS scenario arose before moving towards the high fidelity DNS. An initial geometrical configuration, boundary conditions and flow parameters like turbulent Reynolds number, bulk velocity at the inlet, reference temperature and fluid properties can be used from the above-discussed finalised case of Shams et al., as the beginning point for this work. And optimum case for PTS with buoyancy effects has to be designed.

6

PTS with buoyancy effects case design

This chapter will discuss the study that is conducted for the design of well-defined and calibrated numerical case for the PTS with buoyancy effects. This case will be used for the high-fidelity DNS which will be performed using Nek5000 code. The designing of this benchmark case requires a very independent and thorough study of various flow parameters and boundary conditions. Unlike the previous study of PTS without buoyancy effects, time evolution of the flow properties and the flow behaviour is required to study the flow mixing and evolution of thermal plumes in numerical simulations of the PTS with buoyancy effects, which made it a long duration and computationally challenging project. It is very crucial to find the optimum case which isolates the important phenomena of interest and represents the realistic flow scenario which should also be feasible for the DNS. This is done by means of studying the effect of various boundary conditions and geometrical dimensions of the physical domain and suggesting the optimum ones.

In the following Sections, 6.1 to 6.5, the initial physical domain, mesh properties, description of simulation code, boundary conditions and flow properties are discussed.

6.1. Physical domain

The computational domain represents the simplified reactor pressure vessel with cold leg, downcomer, RPV wall and core barrel wall. The most severe PTS scenario occurs during the injection of cold emergency core cooling (ECC) water into the cold leg during a loss-of-coolant accident (LOCA). This injected water moves towards the reactor pressure vessel and eventually descends in the downcomer while mixing with the downcomer's hot water. During this flow mixing, quasi-planar buoyant plumes are formed. These plumes are at lower temperature then background and are unsteady in nature and their direct contact with the core barrel wall can lead to thermal stresses in it. The mixing in the downcomer and evolution of these buoyant plumes form the major interest of this numerical study. Only a small portion of the realistic downcomer size is considered for the physical domain to reduce the computational requirement for the simulations.

The starting configuration is taken from the case of PTS without buoyancy effects with the incorporation of all the recommendations suggested by Shams et al. [8], discussed in the Section 5.1.4. This geometrical dimensions represents only a portion of actual downcomer and were calibrated based on the flow behaviour without considering the buoyancy effects. Therefore, further calibration of this geometry is required and will be performed based on the flow mixing in the downcomer and the evolution of thermal plumes. The Figure 6.1 represents the physical domain of PTS design. And the Table 6.1 discuss the various geometrical parameters and the consideration made during the selection of them. It is important to notice the changes in the geometry from the one discussed in Section 5.1.1, notice the square leg which is modified from the circular cold leg. Also the motivation behind keeping Inlet-2 is changed, in contrast to PTS without buoyancy effect case.

The domain has two inlets, Inlet-1 for cold injected water (at 293K) and Inlet-2 for relatively hot water (at 353K). With the progression of time the whole domain will get colder because of the injected

cold water and this necessitates the requirement of Inlet-2. A constant addition of hot water from Inlet-2 will keep the temperature difference between the injected cold and hot water of downcomer (upto some extant), which is necessary for the formation of buoyant plumes. In addition to fluid domain, there are surrounding solid domain in the downcomer region, which represents the RPV wall and the core barrel wall.

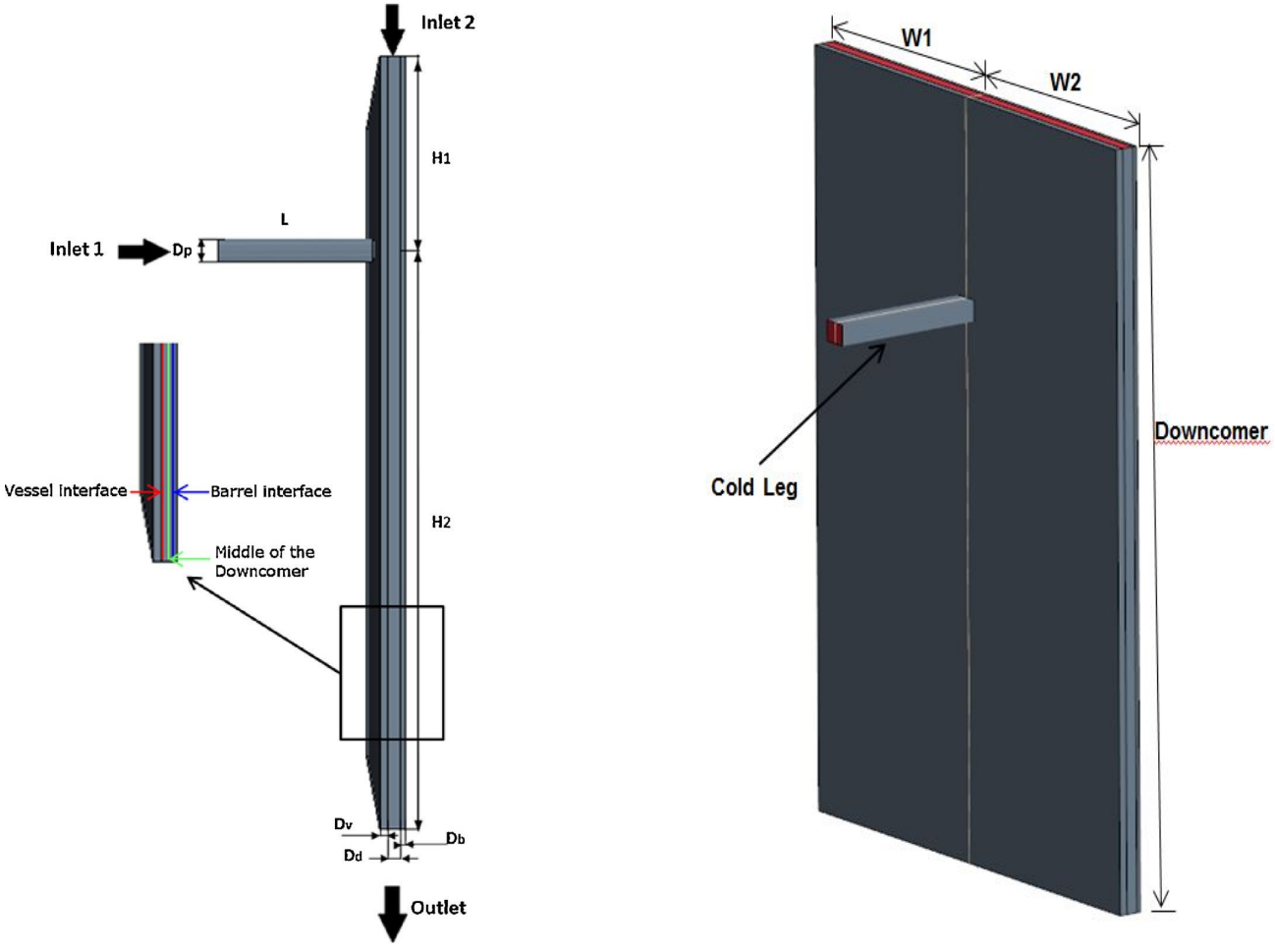

(a) Side view (b) Isometric view

Figure 6.1: Physical domain of PTS Design, finalised by Shams et al. [8].

Parameter	Description	Considerations
Inlet-1	Cold water inlet	Inlet for the ECC (cold) water injection
Inlet-2*	Hot downcomer water inlet	In actual scenario there is no such inlet. This inlet, with hot water addition, is considered to prevent the whole domain to become colder with progression of time and prevent the mixing of flows and formation of plumes.
D_p^*	Width or height of the cold Leg	Same as ROCOM facility's experimental setup.
L	Cold Leg Length	Distance from ECC injection and the downcomer inlet of the ROCOM facility.
H_1^*	Upper height	Height for the development of the flow from Inlet-2.
H_2	Downcomer height	The initial height of downcomer is adopted from Shams et al. [8] case study. This height was found to be optimum for the thermal development of flow fields.
W_1^*, W_2^*	Half width of the geometry	The initial width was adopted from the Shams et al. [8] case study.
D_d	Thickness of the Downcomer	Same as ROCOM test facility setup.
D_v	Thickness of the RPV wall	A 1:5 scale of an actual reactor vessel design.
D_b	Thickness of thecore barrel wall	A 1:5 scale of an actual reactor vessel design.

Table 6.1: PTS Design geometric parameter and their description. ($*$) represents the difference in dimensions and reason in dimension from previous configuration, part of it adopted from [8]

Parameter	Non-dimensionalised by D_p
D_p	1
L	7
H_1^*	10
H_2	23.3
W_1^*	10
W_2^*	10
D_d	0.48
D_v	0.33
D_b	0.16

Table 6.2: Geometric dimensions of the selected PTS design.
(*) represents the change in dimensions from the past study.

The geometric dimensions of each parameter is given in Table 6.2. For coherence in the study, the dimensions of the parameters are non-dimensionalised by the cold leg width (D_p= 0.15), as $x^*= x/D_p$.

6.2. Meshing

A hexahedral trim mesh is used to form the grid to perform the RANS simulations of the PTS configuration. In order to properly resolving the large graidents near the wall and heat transfer to the wall, prism layers are used near the wall. For this purpose, wall y+ is kept around 0.9 (< 1). The mesh structure of the PTS geometry is shown in the Figure 6.2 The barrel domain, vessel domain and fluid domain has 1 million, 1.4 million and 5.8 million mesh elements respectively.

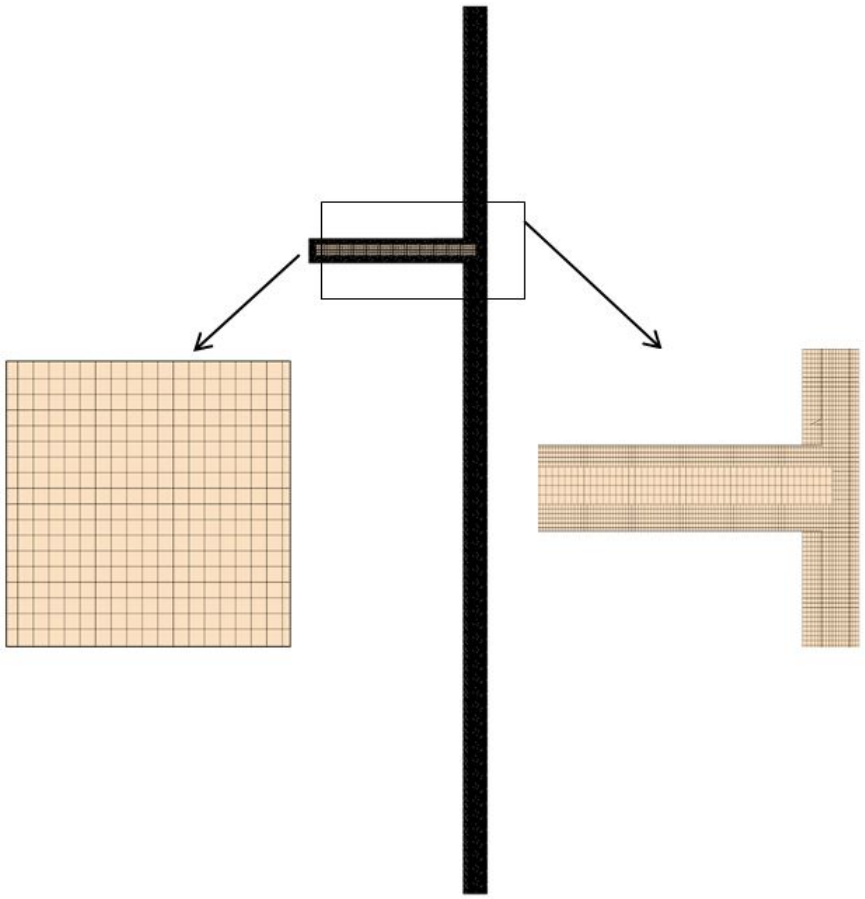

Figure 6.2: Mesh Representation.

6.3. Simulation setup

The simulations for this work are performed using Star-CCM+. URANS turbulence modelling method is used for this numerical study, using non-linear cubic formulation of the low-Reynolds $k-\epsilon$ turbulence model. Boussinesq model which uses Boussinesq approximation, discussed in the Section 3.2, is used with constant density and constant flow properties. For the spatial discretization, second order upwind method is used. And for time discretization, second order implicit method is used, with the time step size of 10^2 seconds. In general, the simulations were studied for the physical time of 15 seconds, based on the formation and evolution of plumes this duration was found appropriate. However, some simulations required longer duration. Star-CCM+ uses unsteady SIMPLE algorithm for the transient analysis, when the implicit method is used along with the segregated flow model for solving the flow equations.

6.4. Boundary conditions

Based on the turbulent Reynolds number of 180, the bulk velocity of 0.0134 m/s at Inlet-1 (see Figure 6.1a) is used. The bulk Reynolds number (Re) is correlated to friction Reynolds number (Re_τ) and is expressed by Dean's correlation as:

$$Re_\tau = 0.175\left(\frac{Re}{2}\right)^{0.875} \tag{6.1}$$

For the Inlet-2 (see Figure 6.1a), a bulk velocity of 0.00134m/s (10% of U_1) is used. As discussed earlier, the role of this inlet is the steady addition of hot water in the domain which should not affect the mixing in the downcomer. Therefore, the velocity finalised in Shams et al. [8] study is used. A

static pressure of 0 Pascals is applied at the outlet. The temperature of injected cold water at Inlet-1 is 293K and hot water from the Inlet-2 is 353K. No-slip wall boundary conditions are applied on the walls. In addition, periodic wall boundary condition is imposed on the spanwise walls of the domain and condition of conjugate heat transfer (CHT) was used at the RPV wall and core barrel wall interfaces.

6.5. Flow properties

The realistic single phase PTS scenario involves hot and cold water mixing, therefore water is used for the fluid domain. dwAs the Boussinesq approximation with incompressible Navier-Stokes equation is used, constant flow properties for water is specified for the simulation. The properties of the water is taken at the temperature of 353K as it will result in lower Prandtl number of 2.23. As the Prandtl number is directly related to the Batchelor length and Kolmogorov length scales, lower Prandtl number corresponds to less mesh refinement requirement. For the solid domains (RPV and core barrel wall) the properties of 16MND5 steel is selected. Since the properties of steel doesn't vary significantly in the range of (293 - 353K), the standard properties at 323K is used. The properties of fluid and solid used for this study are same as used in study of PTS without buoyancy effects and are given in Table 5.3.

6.6. Organisation of the work

Beginning from the geometry and boundary conditions discussed in Sections 6.1 and 6.4 respectively, some initial simulations were performed to observe the phenomena similar to experimental observations. First the cold leg was removed which is discussed in Section 6.7. To find the optimum geometrical dimensions of the downcomer, height (Section 6.8.1) and width calibrations (Section 6.8.2) were performed successively. Once the geometry is finalised, the wall boundary conditions are compared in Section 6.9. After finalising the geometry and boundary conditions, length scale study was performed which is given in the Section 6.10.

6.7. Cold leg removal

Similar to the ROCOM experiments with low velocity current, i.e buoyancy driven flow scenario, the occurrence of the stratification was observed in the cold leg. The stratification is due to the difference in density of the incoming cold and already present hot water in the cold leg. The cold water, owing to its higher density, flows as a separate stream along the lower wall of the cold leg. Also with the Inlet-1 velocity used for the simulations, some regions of recirculating flow were observed in cold leg, which can be noticed in Figure 6.3a and 6.4a. Several simulations with progressively increasing velocity (U_1, 2.5·U_1, 5·U_1, 10·U_1) were performed to understand the relation between the formation of recirculating zones and velocity of the incoming flow from Inlet-1.

It was found that with the increase in velocity, see Figure 6.3a to 6.3d and 6.4a to 6.4d, the stratification of flow streams is reducing along with disappearance of the recirculating zones. From the observation it is apparent that higher flow current from the Inlet-1 forces the already present hot water into the downcomer. Thereby, showcasing the dominating effect of momentum over buoyancy forces. A criterion to distinguish between the momentum-driven and buoyancy-driven, suggested by S. Kliem [2], shows that for a density difference of 2%, a 15% increase in velocity is enough to suppress the buoyancy effects. And the density difference based on the temperature difference of 60 K, used for the simulations, is around 2.1%. The Figure 6.5 shows the velocity magnitude along the height of the cold leg for different inlet velocity cases. The location of the probe is at the middle of the cold leg. The higher velocity close to the lower wall shows the stream of cold water flowing in a separate stream and the stratification. An important observation is the increase in velocity due to the stratification. Since, the cold incoming flow is effectively flowing in a narrow stream it reaches a much higher velocity before entering the downcomer which will result into momentum dominated descent in the downcomer. With the normal inlet velocity, a very pronounced vortex appears at the junction of the cold leg and the downcomer, resulting in a upward movement of the flow towards the Inlet-2. This will eventually result in mixing and recirculation in upper section of the downcomer. Also as a consequence, bigger length of the top section will be required leading to higher number of elements. The velocity at inlet was scaled down in Shams et al. [8] study, considering the feasibility of performing DNS, which aggravated the recirculation in the cold leg.

The aim of this project is to design the numerical case for the buoyancy-driven flow mixing scenario with the major emphasis on the formation and evolution of buoyant plumes in the downcomer. This and DNS feasibility limits the inlet velocity. Considering the above mentioned problems and concerns, a decision to remove the cold leg from PTS physical domain was considered. The inlet is moved to the junction location while keeping the inlet velocity same.

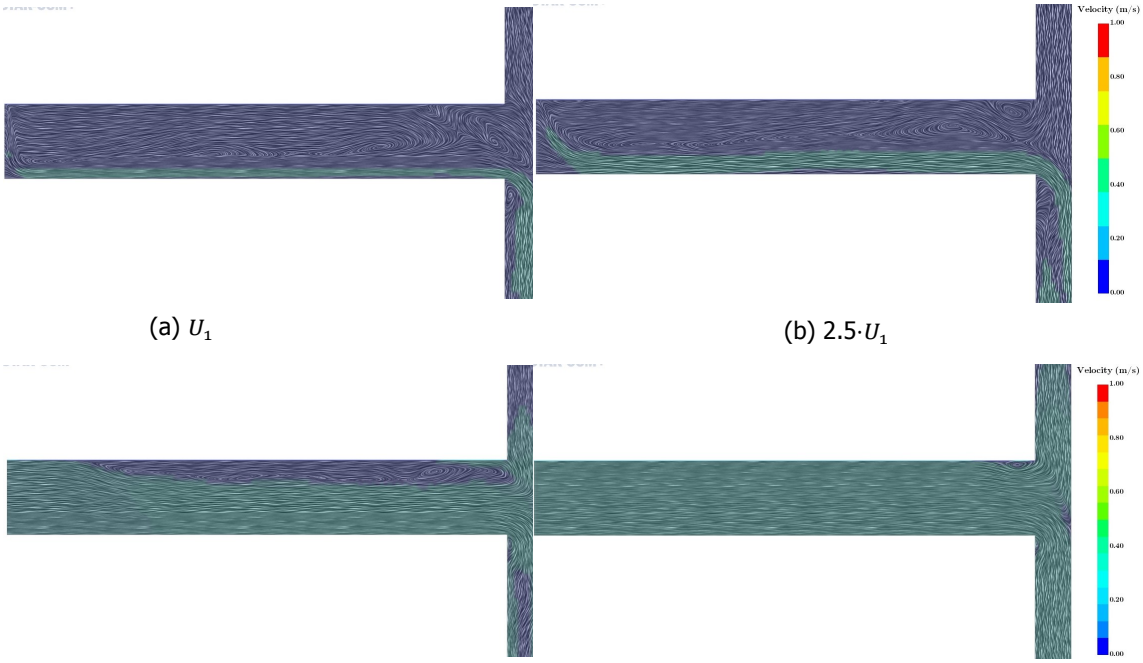

(a) U_1 (b) $2.5 \cdot U_1$

(c) $5 \cdot U_1$ (d) $10 \cdot U_1$

Figure 6.3: Iso-contours of velocity in the cold leg. The velocity is varying between 0 and 1.

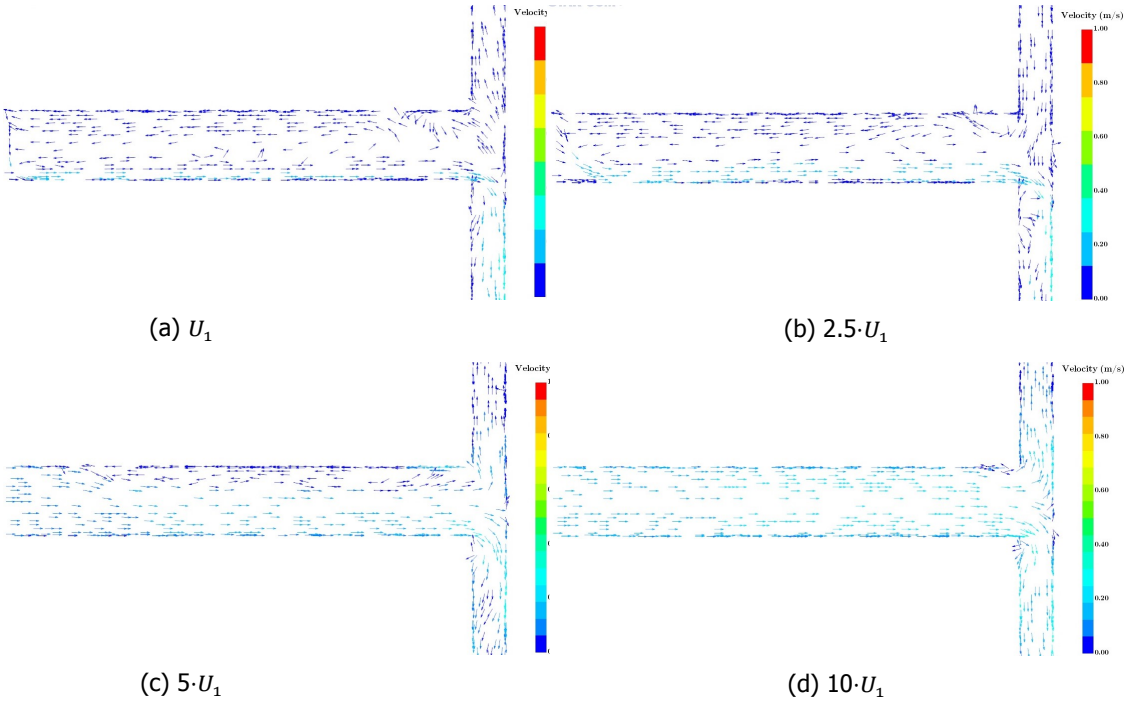

(a) U_1 (b) $2.5 \cdot U_1$

(c) $5 \cdot U_1$ (d) $10 \cdot U_1$

Figure 6.4: Glyphs of velocity in the cold leg showing the velocity magnitude's direction at different point. The velocity is varying between 0 and 1.

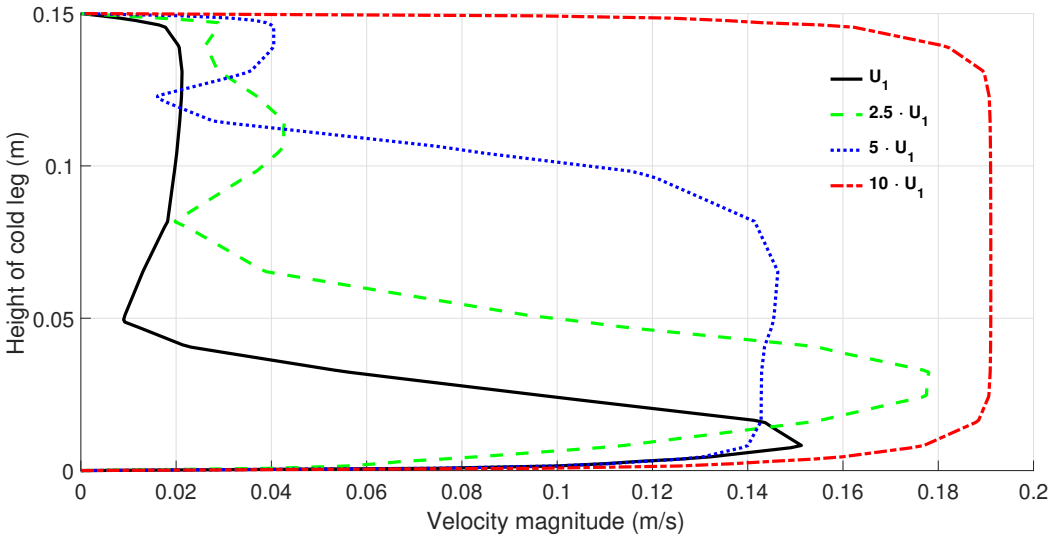

Figure 6.5: Velocity variation at the middle of the cold leg for different Inlet-1 velocity

6.8. Geometry calibrations

Performing numerical simulations on the actual full scale size of downcomer is challenging considering the computational time and requirement. Therefore, a feasible enough physical domain which can reproduce the phenomenon of interest has to be calibrated. The height of the lower section and width of the downcomer is calibrated.

6.8.1. Height of the Downcomer

Only a section of a full scale height of the downcomer is considered for the numerical simulations. The aim was to find the optimum height, which can provide enough length for mixing of the flow and the formation of independent buoyant plumes. It is important to understand that in the scenario of low inlet velocity, where the buoyancy effects are dominated, the flow will descend in the downcomer forming these independent plumes which detaches from the main stream and evolve in the downcomer. Study of these plumes and their movement across the downcomer forms the main background of the PTS with buoyancy effects case design process as these plumes comes in direct contact with the core barrel wall.

For the calibration process, simulation with three different height of downcomer's lower section, H_2, see Figure 6.1a, were performed. The different heights are H_2, $H_2 + 3D_p$ and $H_2 + 6D_p$. Here D_p is the width of the cold leg, see Figure 6.1a, and the height increment is performed in terms of it for better coherence. As only the effect of the height of downcomer had to be studied, all the boundary conditions and initial conditions were kept constant. The Figure 6.6 shows the evolution of temperature at the middle plane of the downcomer with time, which was used to study the difference in the flow descent for different height. Since, the mixing in the downcomer and descent of flow is a transient process, the variation in the temperature profile had to be studied at various time steps.

In general, when the injected cold water descends in the downcomer it falls in the form of a small streamline while mixing with hot water. The mixing depends on the height of the downcomer, larger height will provide more time and distance for mixing. Therefore, sufficient distance of the outlet is important for achieving the realistic mixing scenario. For the case with height, H_2, the streamline is attached to the outlet for most of the duration, which suggested the need of increasing the height. It can be noticed in $H_2 + 3D_p$ height case that the descending cold water stream gets detached from the outlet and starts to oscillate freely. This will result in formation of smaller independent buoyant-plumes. Similar effect can be seen in the case with $H_2 + 6D_p$ height of downcomer. In both of these cases it can be concluded that the outlet is sufficiently far enough from the main mixing region therefore less influence of the outlet boundary conditions on the mixing. However, the height $H_2 + 6D_p$ requires significantly higher mesh elements which eventually will require higher computational time. Therefore, height of the downcomer, $H_2 + 3D_p$, is finalised for the DNS simulation.

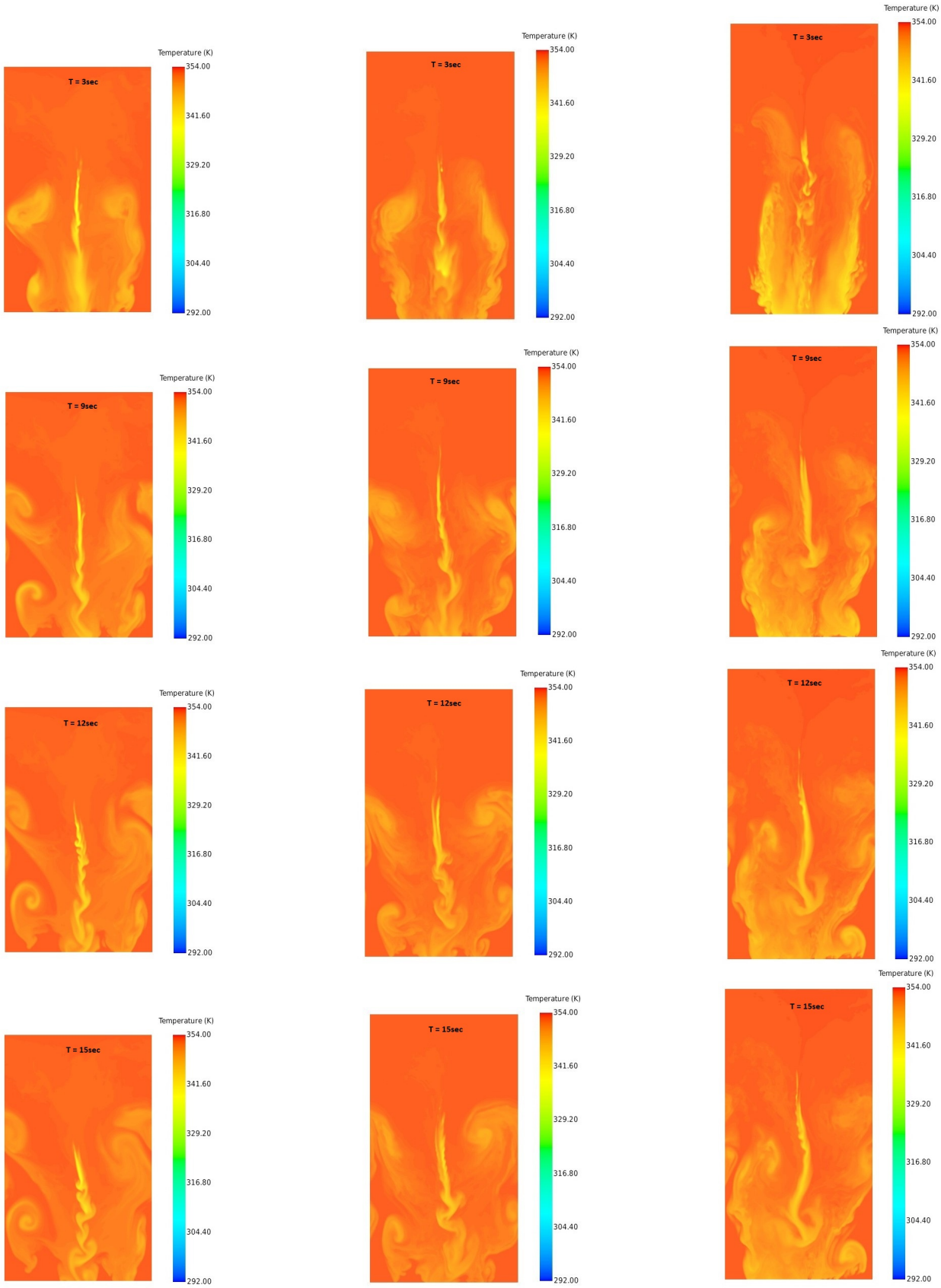

Figure 6.6: Time evolution of temperature of flow, at midplane of the downcomer, for different height of the downcomer. Left column is with height (H_2), middle is with height ($H_2 + 3D_p$) and the right column is with height ($H_2 + 6D_p$).

6.8.2. Width of the Downcomer

Since the downcomer is the region surrounding the whole of the RPV, the selection and calibration for the optimum width of the downcomer also becomes important. Two different downcomer width, viz. W_1, W_2 and $W_1 + 2d_p, W_2 + 2d_p$, have been selected for the comparison. With a wider width the formed plumes has larger domain to evolve and mix. The important reason behind increasing the width was to keep the side boundaries far from the mixing zone so as to have a less influence of the boundary conditions on mixing. The temperature variation in the mid section of the downcomer at different time steps are shown in Figure 6.7. It was observed that the descending cold stream mixes in a similar way for both configurations. Even for the wider domain the plumes evolves and reach the side boundaries. Because of this reason, the periodic boundary condition is considered. However, the computational time for the wider domain increases significantly. Therefore, the width of the physical domain was finalised to be W_1, W_2.

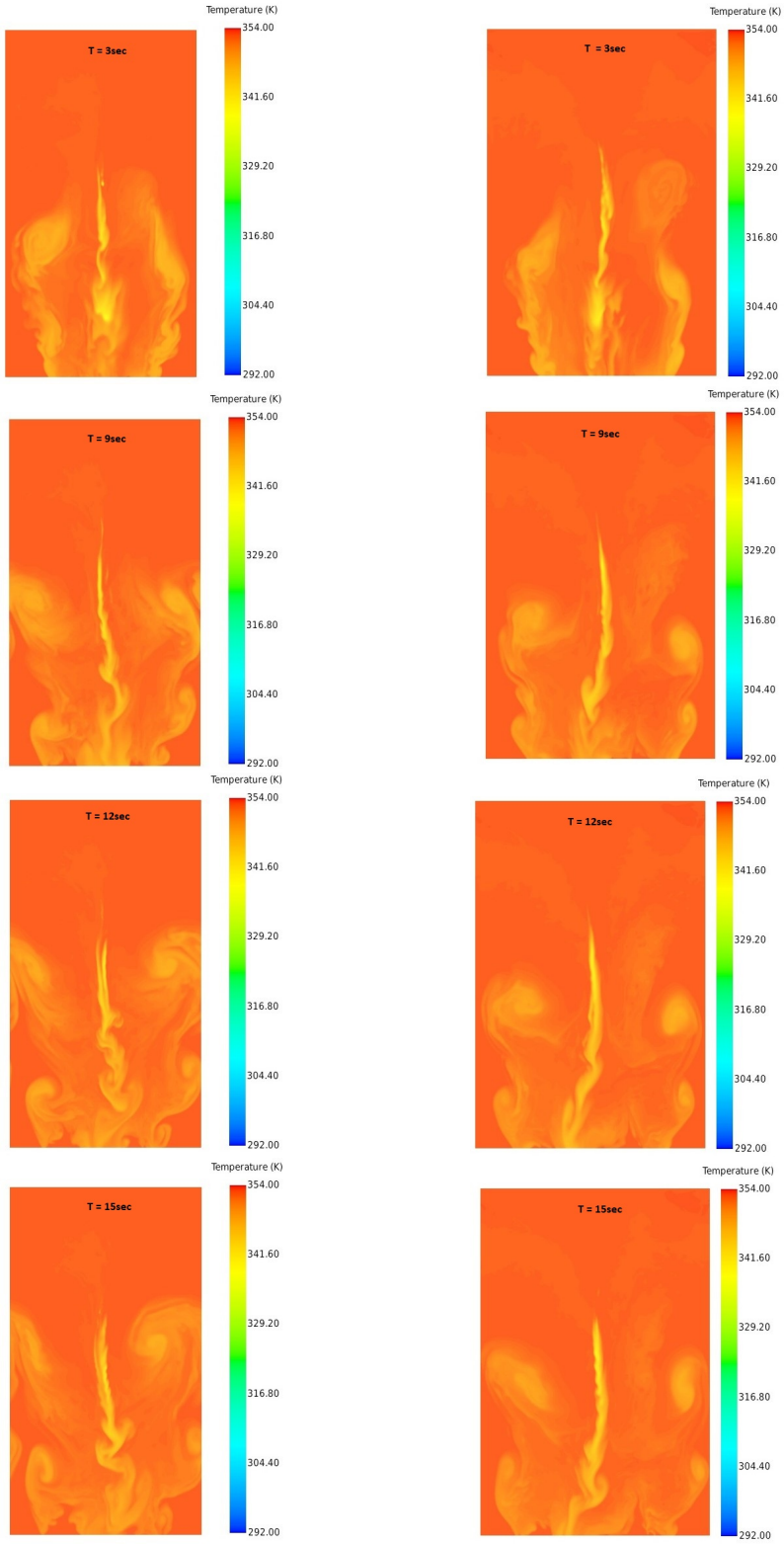

Figure 6.7: Time evolution of temperature of flow, at midplane of the downcomer, for different width of the downcomer. Left column is with width (W_1, W_2) and right column is with width ($W_1 + 2D_p, W_2 + 2D_p$)

6.9. Boundary conditions study

As the downcomer is surrounded by walls on the both sides, i.e. RPV wall and core barrel wall, the choice of boundary condition on the interface has an important implication on the flow mixing and temperature variation in the downcomer. Three different wall boundary conditions, i.e. conjugate heat transfer (CHT), adiabatic and isothermal, were studied. The location of the line probes is shown in Figure 6.8a. The distance of line probe 1 and 2 is equal to $7D_p$ and $10D_p$ respectively. The temperature variation across the wall and fluid domain, for the three different boundary conditions, at two line probes location are shown in the Figure 6.10. Also the Figures 6.8b, 6.9a, and 6.9b, shows the temperature profile at the side view of downcomer's mid section, barrel interface and vessel interface respectively, for the case with CHT boundary condition. All the above mentioned plots and figures are shown at the time step of 9 sec. Similar results were observed for the other time steps.

As the cold water falls as a stream attached to the vessel interface, more heat transfer between the vessel wall and the fluid will occur for the case with CHT boundary condition, which can be noticed in the Figure 6.10. The region near the inlet has the large gradient of temperature between wall and the fluid resulting in higher heat transfer. Therefore the line probe 1, which is near to the inlet, shows a lower temperature around the vessel interface for both the CHT and adiabatic case as compared to the line probe 2. Since the incoming cold water doesn't interact with the core barrel wall directly, all the three boundary conditions show similar temperature for the first line probe. At the second line probe location, the colder plumes have interacted with the barrel wall leading to difference in the temperature for the three boundary conditions around the barrel interface. For the isothermal boundary condition case the temperature at both the wall interface reaches 353K. A significant different temperature variation can be observed for all the three cases. However, it is important to consider the significant increase in mesh elements and consequently the computational time required for the DNS with CHT between solid and fluid domain.

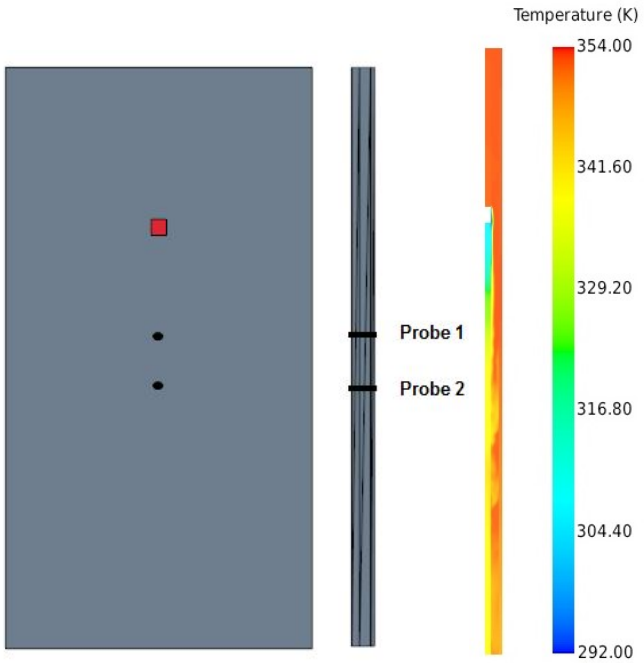

(a) Line probes location

(b) Side view of mid Section of Downcomer

Figure 6.8: Temperature profile along with the line probe location .

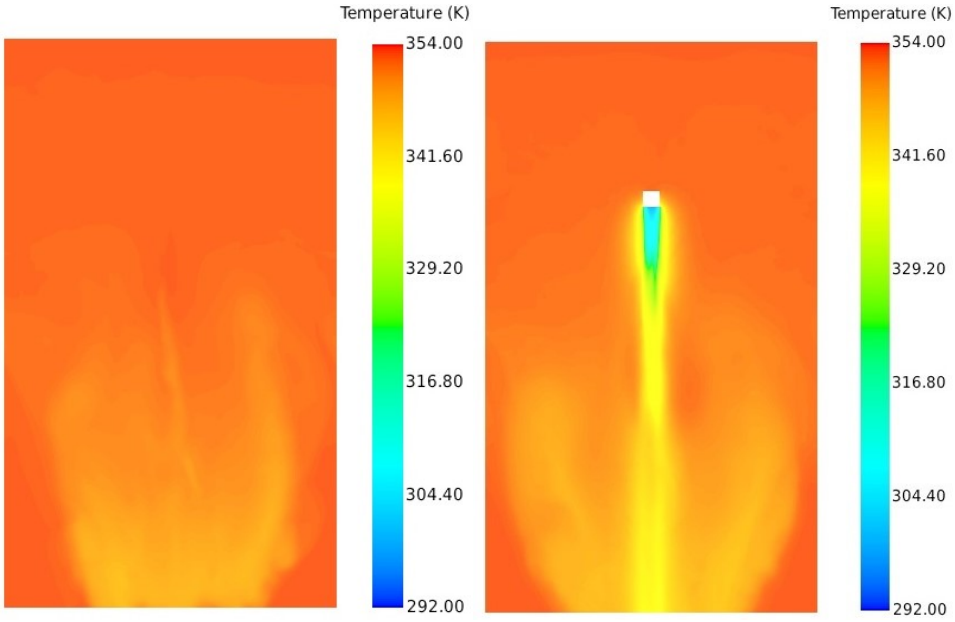

(a) Core barrel interface (b) RPV wall interface

Figure 6.9: Temperature profile at the wall interfaces.

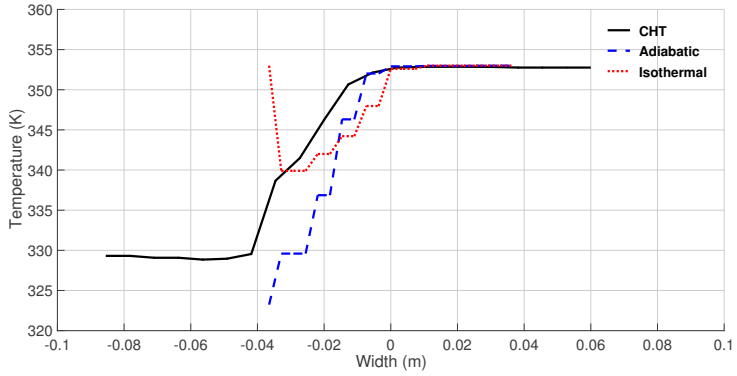

(a) Line probe 1

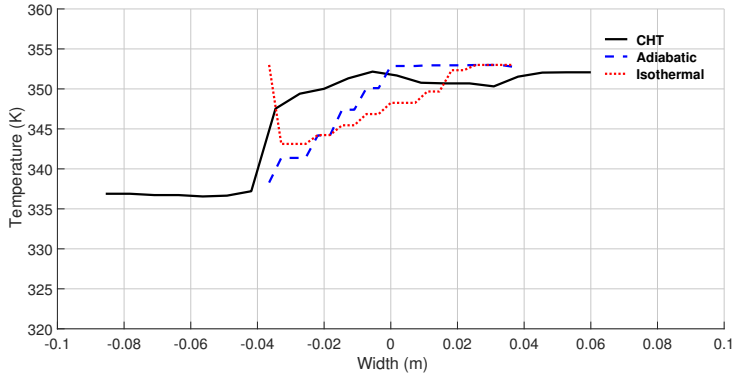

(b) Line probe 2

Figure 6.10: Temperature variation along the line probe for different boundary conditions at time step = 9 sec.

6.10. Length scales study

Length scales are the indicative of the smallest eddies present in the flow, the scale at which the energy is dissipated. For the better estimation of the mesh for DNS, knowledge of the region with smallest scales is essential. With the proper refinement of mesh it will become possible to resolve the smallest scales with DNS.

Since the RANS simulations are performed, two different mesh configuration were used to check the dependency of the solution on the mesh refinement. Original mesh consisting of 5.8 million mesh elements and a finer mesh with 10 million mesh elements were used for the simulation. A good agreement between the turbulence dissipation rate and hence the scales was observed with both mesh configurations. Therefore, the original size of the mesh is used for the length scale study as it requires less computational time.

The Kolmogorov (η) and Batchelor (η_B) length scales were estimated by using their respective classical formulae and are non-dimensionalised by the ratio of friction velocity (u_τ) and kinematic viscosity (ν) as follows

$$\eta^+ = \left(\frac{\nu^3}{\epsilon}\right)^{1/4} \frac{\mu_\tau}{\nu}, \tag{6.2}$$

$$\eta_B^+ = \left(\frac{\alpha^2 \nu}{\epsilon}\right)^{1/4} \frac{\mu_\tau}{\nu}, \tag{6.3}$$

where α is the thermal difusivity and ϵ is turbulence dissipation rate.

The Figure 6.11 and Figure 6.13 shows the non-dimensional Kolmogorov and Batchelor length scales at the barrel interface, mid section of the downcomer and the vessel interface respectively. It can be observed that the smallest scales forms in the region where the cold water's stream is descending in the downcomer. Since the smallest scales were along the descending streamline, three line probes were used to understand the variation of scales size along the mid section of downcomer at each above-mentioned plane, shown in Figure 6.12 and 6.14. The sudden jump in the scales magnitude at the vessel interface is due to the presence of the inlet, where the incoming flow in uniform. At the top of the downcomer there is a constant inflow of hot water and as the flow is rather uniform, the largest scales are present in that region. A clear distinction between Kolmogorov and Batchelor scale can be seen based on the smallest scale's size. As the Prandtl number based on the reference temperature (353K) was 2.2, smaller Batchelor length scales were expected. The largest Kolmogorov and Batchelor scales were of the order $\approx$ 3.5 and 3 respectively. Since the mixing process is transient in nature, the location of smallest scales will vary at each time step. However, the above magnitude gives an approximate estimate of the mesh refinement required for the DNS.

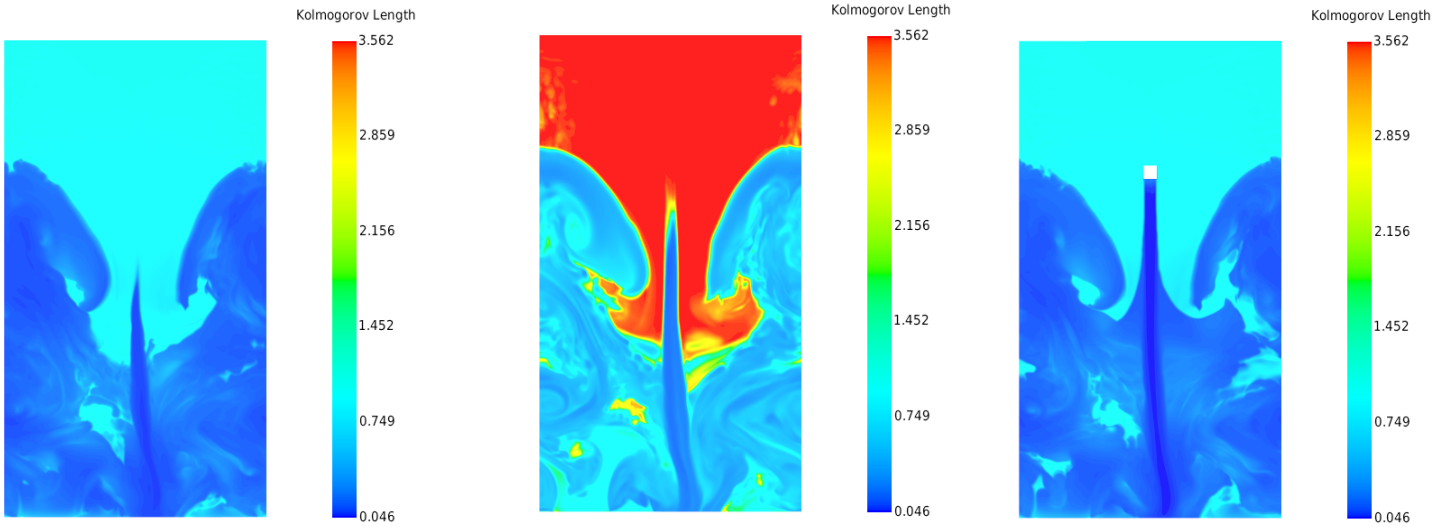

(a) Barrel interface (b) Downcomer's mid section (c) Vessel interface

Figure 6.11: Non-dimensional Kolmogorov length scales.

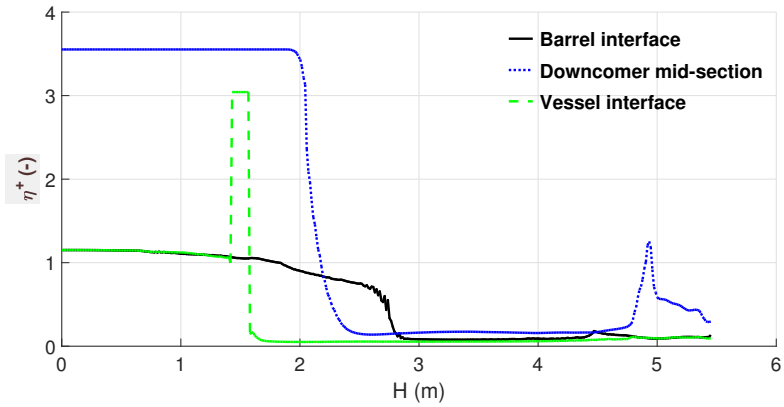

Figure 6.12: Non-dimensional Kolmogorov length scales variation along the height of the downcomer. Height varies from top to bottom while moving from left to right in the plot.

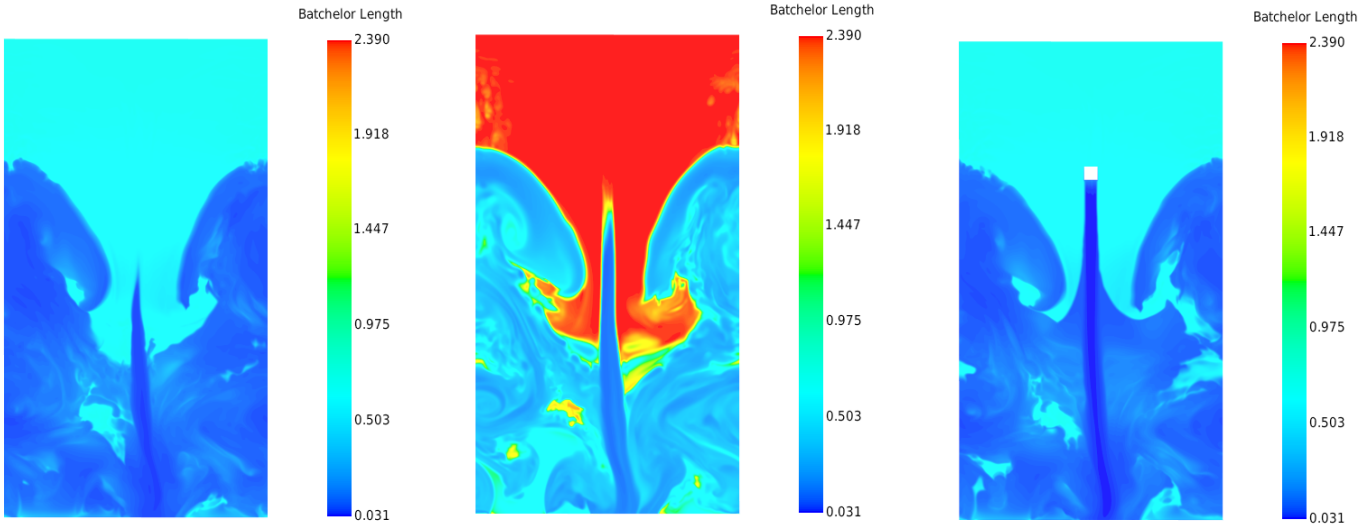

(a) Barrel interface (b) Downcomer's mid section (c) Vessel interface

Figure 6.13: Non-dimensional Batchelor length scales.

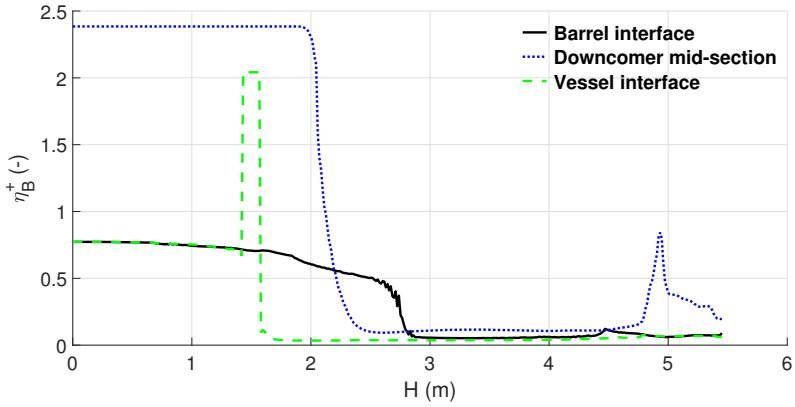

Figure 6.14: Non-dimensional Batchelor length scales variation along the height of the downcomer. Height varies from top to bottom while moving from left to right in the plot.

6.11. Summary

Following our research question, a study has been performed for designing an optimum numerical case for the PTS with emphasis on buoyancy driven flow mixing in the downcomer. Several observation were seen and consequently some modifications in the PTS design and the flow conditions were made. It was observed that the Inlet-2 with constant inflow of hot water is required to create a temperature difference between the mixing flows. The cold leg has to be removed to be able to perform DNS, because of the stratification and consequently momentum driven flow descent in the downcomer. The optimum height and optimum width of the downcomer was finalised to be $H_2 + 3D_p$ and $W_1 + W_2$, see Table 6.1, respectively. Periodic boundary conditions is suggested at the spanwise walls because of the movement of thermal plumes, which will also be feasible for the DNS. A considerable different temperature variation in the downcomer was observed with different wall boundary conditions. Therefore, a choice has to be made based on the computational time and resources limitation, for using conjugate heat transfer in DNS. In the length scale study, it was seen that the smallest scales are in the region where the cold water streamline is descending in the downcomer and therefore, a very fine mesh will be required in these regions.

7

Rayleigh Bénard Convection validation study

This chapter will present the validation study performed for the Rayleigh Bénard convection case using Nek5000. The case and results selected for the validation is a part of the Kooij et al. [10] work on study of rotating RBC, performed using Nek5000. The case designed in the previous chapter for the PTS with buoyancy effects involves complex phenomena like turbulence, convection and buoyancy driven mixing. Therefore, it becomes important to perform a validation study of a smaller and relevant case before moving towards the DNS of final complex PTS scenario. The RBC case is extensively studied using numerical and experimental simulations in the past and since it involves turbulent convection and buoyancy driven flow mixing, which are the most important phenomenon that occurs in PTS scenario, it becomes a good choice for performing a validation study.

The following sections will discuss the case description and results. Section 7.1 provides a background of the RBC phenomena. Following Sections, 7.2 to 7.6, will discuss the physical domain used for the simulations, mesh configuration, simulation specifications, description of the selected case and the some of the equations used to compute the variables respectively. In Section 7.7 the results of the simulations are discussed with the explanation of the observations. Finally in Section 7.8, the results are compared with the results of the Kooij et al. work and the conclusions are drawn.

7.1. Rayleigh Bénard convection : importance and significance

Thermally driven turbulence is an important natural phenomenon that drives atmospheric circulations and convection in stars and planets. Turbulent thermal convection occurs in industrial processes, which range from the passive cooling of nuclear reactors to the controlled growth of crystals from the melt [28]. Rayleigh Bénard convection (RBC), which consists of a fluid layer heated from below and cooled from above in a vertically bounded domain, is a classical case which forms a basis for understanding the thermal convection and to approach above cases [29]. When the layer of fluid is heated from the bottom and provided a cooler temperature condition at the top, the thermal expansion of the fluid creates a buoyant force which set the fluid in motion and results in convective heat transfer. The force large enough to onset the convective motion is characterised by a non-dimensional parameter callled Rayleigh number.

7.2. Physical domain

For the numerical simulation of RBC scenario a cylindrical cell with aspect ratio (Γ) of 1 is used. Aspect ratio is defined as the ratio of distance between lateral to the vertical extant of the cell , i.e. D/H, see Figure 7.1. It is a cylindrical domain with curved walls with no-slip and adiabatic wall boundary conditiona. There is no inlet or outlet in the domain, in essence no inflow or outflow in the domain. The fluid is bounded from all side. The temperature at the top wall can be represented as T_0 and at the bottom wall as $T_0 + \Delta T$.

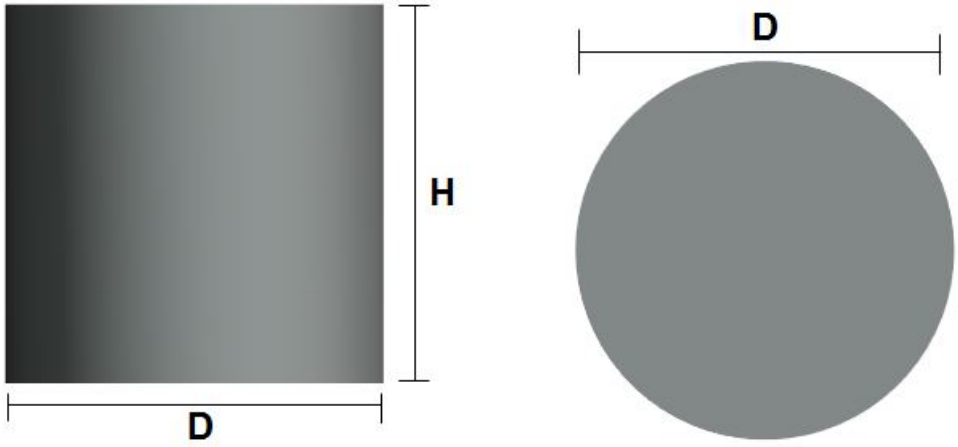

(a) Front view (b) Top view

Figure 7.1: The geometry of the cell.

7.3. Meshing

For performing direct numerical simulation it is essential to have refined mesh to resolve the smallest turbulent scales. Also when the solid boundaries are present in the domain, viscous boundary layers will be generated, which necessitates a refinement in the wall region as well. Therefore, a minimum number of grid points has to be clustered in the wall vicinity. A mesh dependence study had been performed by Kooij et al. [10] for the cases with varying Ra and using the different number of mesh elements in horizontal (xy) and vertical (z) plane. The orientation of the axis are shown in the Figure 7.3a. For the cases with Ra $\leq 10^8$, the finalised number of elements in the lateral and vertical direction is given in Table 7.1. The same number of elements and resolution is used for this numerical study.

Structured grid is used as the spectral elements, a sectional view of it is shown in Figure 7.2. These spectral elements will be further subdivided into grid points based on the polynomial degree used for the simulations and the corresponding mesh is shown in Figure 7.3.

E_z	$\overline{h}_z$	E_{xy}	$\overline{h}_{xy}$
32	3.125E-2	972	2.766E-2

Table 7.1: Mesh Specifications.

where, E_z and E_{xy} is the number of spectral elements in vertical (z) direction and horizontal (xy) plane respectively. $\overline{h}_z$ and $\overline{h}_{xy}$ is the average mesh widths in the z-direction and xy-plane respectively.

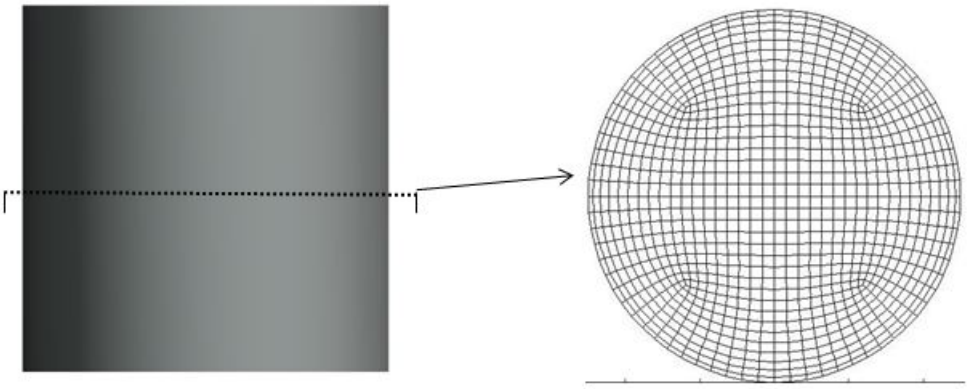

Figure 7.2: Spectral elements distribution in xy plan.

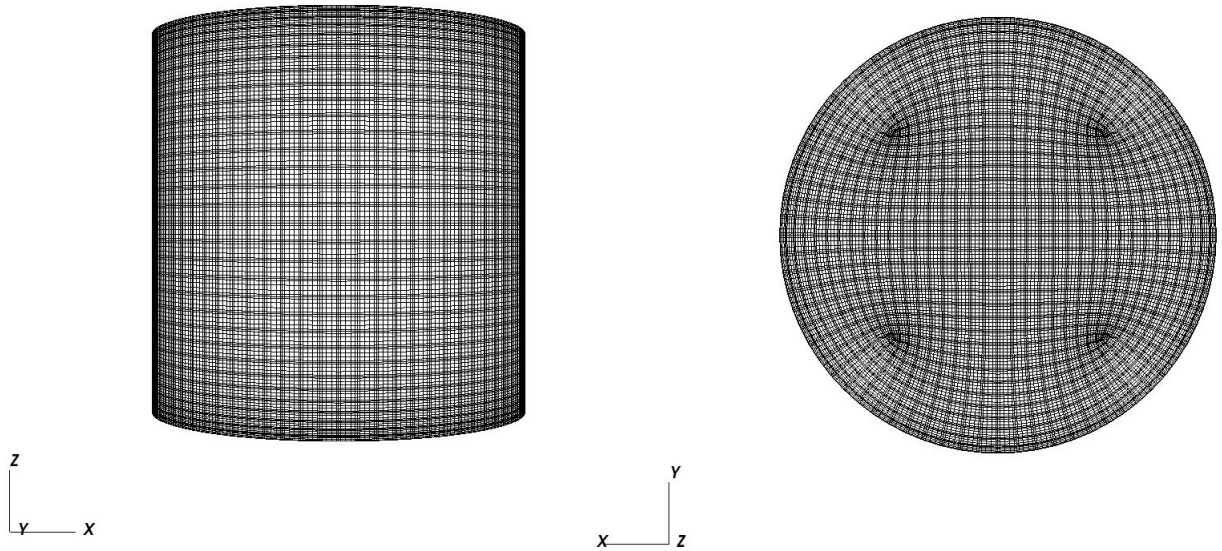

(a) Front view of mesh (b) Top View of Mesh

Figure 7.3: Schematic representation of Mesh after grid points generation.

7.4. Cases description

The Ra $\approx 10^7$ is said to be a transition between soft and hard turbulence, [30]. Therefore, two cases with Ra of 10^6 (soft turbulence) and 10^8 (hard turbulence) are simulated for the validation study. The Rossby number (Ro) = ∞ whcih corresponds to stationary domain is used for both the cases. The Prandtl number of 6.4 is used for both the cases. The governing equations used for this cases, the non-dimensionalised terms and the definition of Ra are given in the Section 3.3.

7.5. Simulation setup

Similar setup as one used by Kooij et al. in Nek5000 is used for the simulation. The basis functions of the velocity are local tensor-product Lagrange interpolants of degree 'p' on Gauss–Lobatto–Legendre nodes, whereas the basis functions of the pressure are Lagrange interpolants of degree 'p-2' on Gauss–Legendre nodes. The total number of grid points is then $(P+1)^3$ (for the velocity) per three-dimensional element. A semi-implicit third-order BDF3/EXT3 time marching scheme is used [27], which is discussed

in Section 4.5.3. Third-order backward differencing scheme (BDF3) with a third-order extrapolation scheme (EXT3) is used to integrate viscous term and the nonlinear convective term respectively. A time step size of 10^{-3} seconds is used for both the cases which corresponded to CFL $\leq$ 0.5 and ensured the stability of the simulations. Quadrature rules of order 3N/2, instead of N, is applied in this numerical study and is suggested a good choice to approximate the skew-symmetry of the convective operator up to machine precision [10]. Spectral elements with polynomial degree p=5 are used. The meshes are refined near the wall to capture the large gradients in the boundary layers. The simulation time of 650 and 700 secs is considered for Ra = 10^6 and Ra = 10^8 cases starting from a zero-velocity field and a linear temperature profile (T = z) as initial conditions respectively. The case with Ra = 10^6 and Ra = 10^8 is time averaged for the duration of 150 seconds and 300 seconds respectively.

7.6. Nussselt number equations

The Nusselt number is a non-dimensional parameter that characterizes the efficiency with which the heat is transported. It is defined as:

$$Nu = \frac{Hh}{\lambda \Delta}, \tag{7.1}$$

where H denotes the heat per unit surface area transferred between the two surfaces, λ is the thermal conductivity, h is the distance between the upper and lower limit of fluid and Δ denotes the temperature difference between upper (cold) and lower (hot) boundary.

The Nusselt Number is the ratio of total and conductive heat flux and can be written in the form of local heat transfer as:

$$Nu = (PrRa)^{1/2} u_z T - \partial_z T, \tag{7.2}$$

Here z is the vertical direction, see Figure 7.3, and gravity is acting in negative direction of z. And T represents temperature.

The purpose of direct numerical simulation is to measure the global heat transfer by the flow. An approach used by Kerr [31] was applied in the numerical studies performed by Kooij et al. [10] and subsequently in his work. The global heat transfer can be measured in two ways, viz. it can be defined from the conductive and convective heat transfer definition as :

$$< Nu >_V \quad = \quad 1 + (PrRa)^{1/2} < u_z T >_V, \tag{7.3}$$

and it can be evaluated by computing the mean heat flux at the hot and the cold walls [9] as

$$< Nu >_W \quad = \quad < \partial_z T >_W, \tag{7.4}$$

where $< . >_W$ and $< . >_V$ denotes the average of quantity taken over the walls and over the volume respectively.

The averages are simplified with the boundary conditions given in Table 7.2, following the approach by Kerr [31]. Since the governing equations are non-dimensionalised in terms of Rayleigh Number and Prandtl number, these boundary conditions are more suitable from the implementation point of view.

Bottom Plate	u = 0	T = 1
Top Plate	u = 0	T = 0
Side Wall	u = 0	$\frac{\partial T}{\partial n}$ = 0

Table 7.2: Dimensionless Boundary Condition.

7.7. Results

7.7.1. Flow Topology

As discussed earlier, the flow sets in to motion as a result of the buoyancy forces which are generated due to thermal gradient. However, the flow topology and the way flow mixes depends on the Rayleigh number. In the literature, a clear distinction between the flow structures and patterns are discussed

for the different Ra regime. In this Section only the one relevant, i.e. Ra $\leq 10^9$ and the flow topology of the simulations performed will be discussed.

A schematic representation of the generalised flow scenario for Ra $\leq 10^9$ is shown in the Figure 7.4. Large-scale structures characterizes this flow scenario which influence the viscous and thermal boundary layers. Basically, the flow scenario is complex with a mean flow structure, which depends on the Rayleigh number, and the large-scale recirculation. The mean flow consists of the superposition of two counter-rotating toroidal rings attached to the horizontal plates and the large-scale recirculation, as can be seen in Figure 7.4, [9]. For understanding of the flow motion, isocontour of the temperature field and the vertical velocity fields at different time steps for the two cases, i.e. Ra = 10^6 and Ra = 10^8, are shown in Figures 7.5 and 7.6 respectively. These axisymmetric rings make the fluid at the hot (cold) plate to raise (descend) along the lateral wall and to descend (raise) at the cell axis, see Figures 7.5a and 7.6a. Due to this motion, thicker boundary layer will be formed in the radial direction and the thinnest layer will be present at the centre of the cell. In total, the overall mean flow is composed of the features of the circular toroidal rings, the large-scale recirculation and the flow structures form due to their interaction. For Ra = $2 \cdot 10^6$ it was observed by R. Verzicco [9] that the wall region is dominated by the axisymmetric toroidal rings whereas the bulk is influenced by the asymmetric large roll giving rise to hot current on one side and descending current for the cold fluid on the other side, similar observations were seen in the Figure 7.5c and 7.6c.

The most prominent structure in turbulent convection is the thermal plume, these are the localised volume of fluid at a temperature different with the background [32]. A large amount of heat is transported across the convection cell by means of these thermal plumes [33]. For Ra ($\leq 10^6$) larger and smoother plumes emerges from the turbulent background. With the increase of Ra to 10^8, the emerging plumes becomes smaller and less coherent because of the increase in the intensity of turbulence. And this plumes detaches from the respective top and bottom plates and accelerates towards the bulk of the flow under the action of buoyancy forces and finally impinge on the opposite wall [34]. Towards the center region of the cell, thermal plumes have a mushroom-like shape, whereas close to the walls they have a sheet-like structure, see Figure 7.5. The sheet-like plumes form a fine network across the plates and at their intersection spots, the mushroom-like plumes emerges. The intersection of different sheet-like plumes results in a large concentration of momentum which in combination with the buoyancy forces leads to ejection of mushroom-like plumes [34]

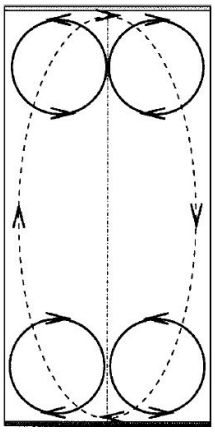

Figure 7.4: Schematic representation of mean flow arrangement, (- - - - -) for weaker structure, (——-)for most intense structure, adopted from [9].

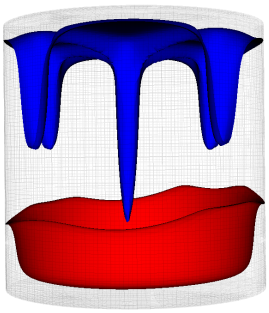

(a) Ra = 10^6 at 100sec

(b) Ra = 10^8 at 100sec

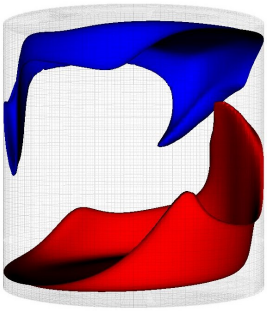

(c) Ra = 10^6 at 200sec

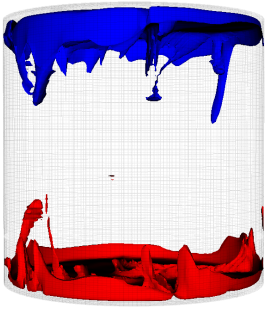

(d) Ra = 10^8 at 200sec

Figure 7.5: Iso-surface of the temperature field for different Rayleigh numbers. Red and blue color represent normalised temperature T = 0.65 and T =0.35 respectively

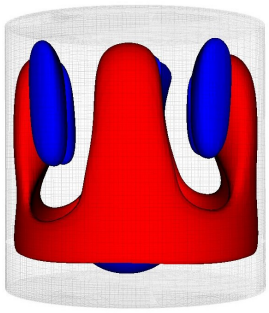

(a) Ra = 10^6 at 100sec

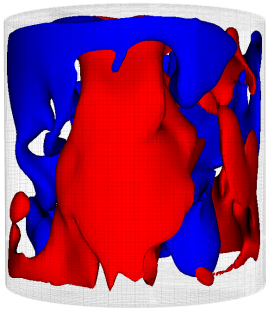

(b) Ra = 10^8 at 100sec

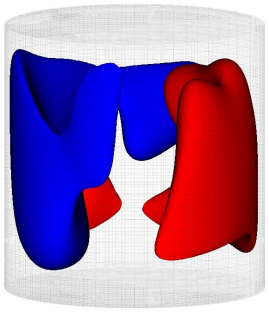

(c) Ra = 10^6 at 200sec

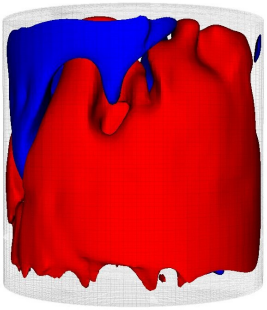

(d) Ra = 10^8 at 200sec

Figure 7.6: Iso-surface of the vertical velocity field for different Rayleigh numbers. Red and blue color represents u_z = 0.07 and u_z = -0.07 respectively.

7.7.2. Nusselt number computation

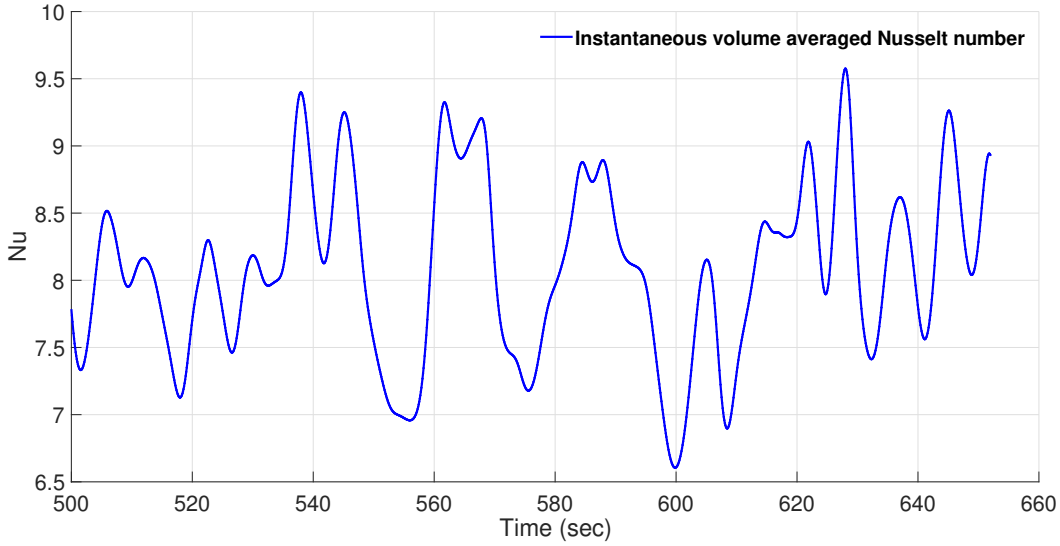

(a) Instantaneous volume averaged Nusselt number.

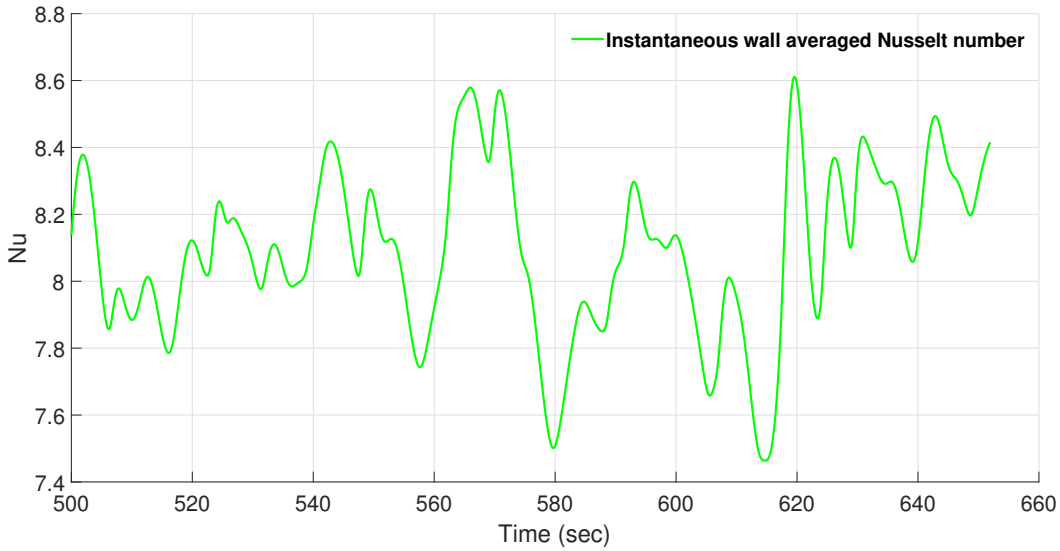

(b) Instantaneous wall averaged Nusselt number.

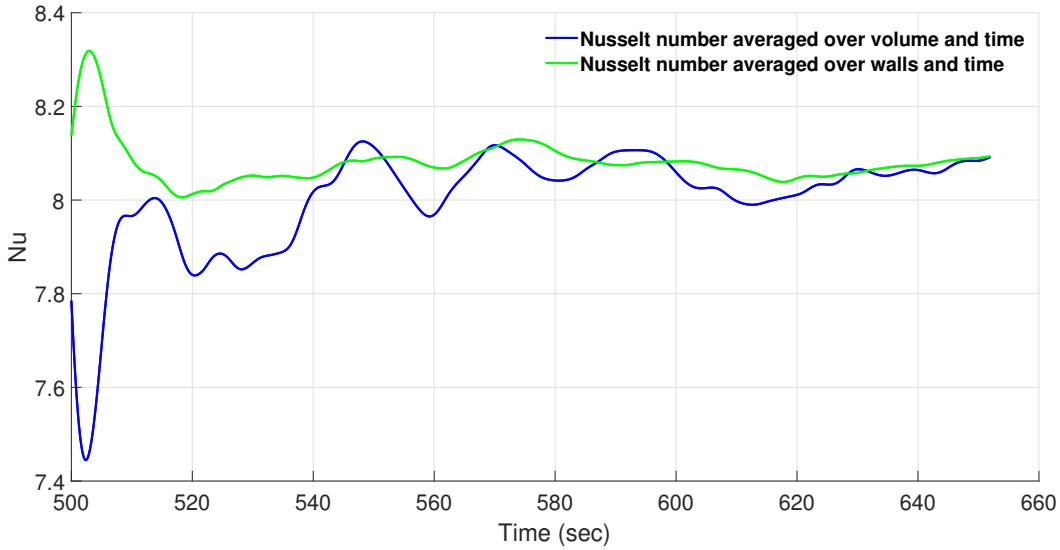

(c) Time averaged Nusselt number's convergence

Figure 7.7: Plots of computed wall and volume averaged Nusselt number for Ra = 10^6.

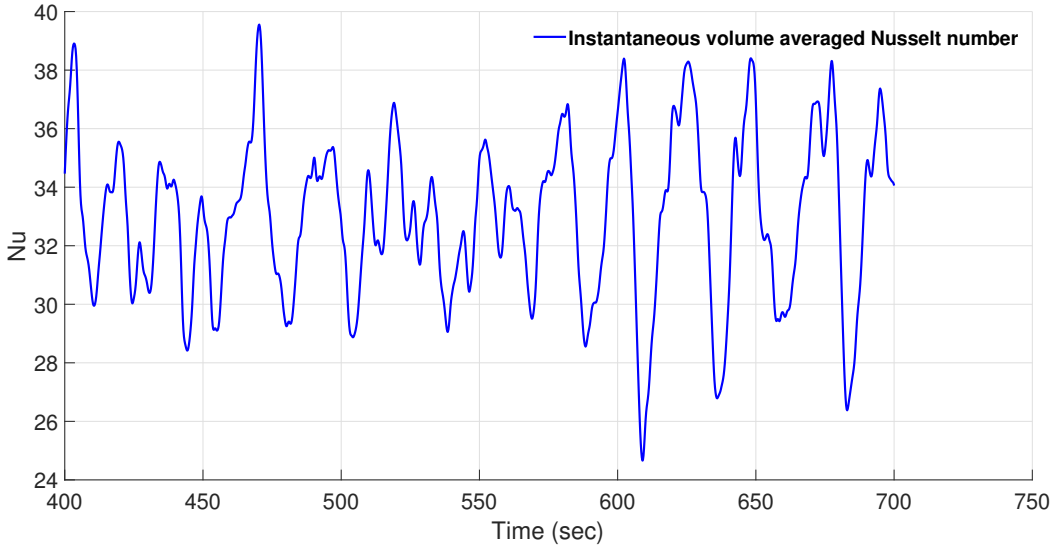

(a) Instantaneous volume averaged Nusselt number.

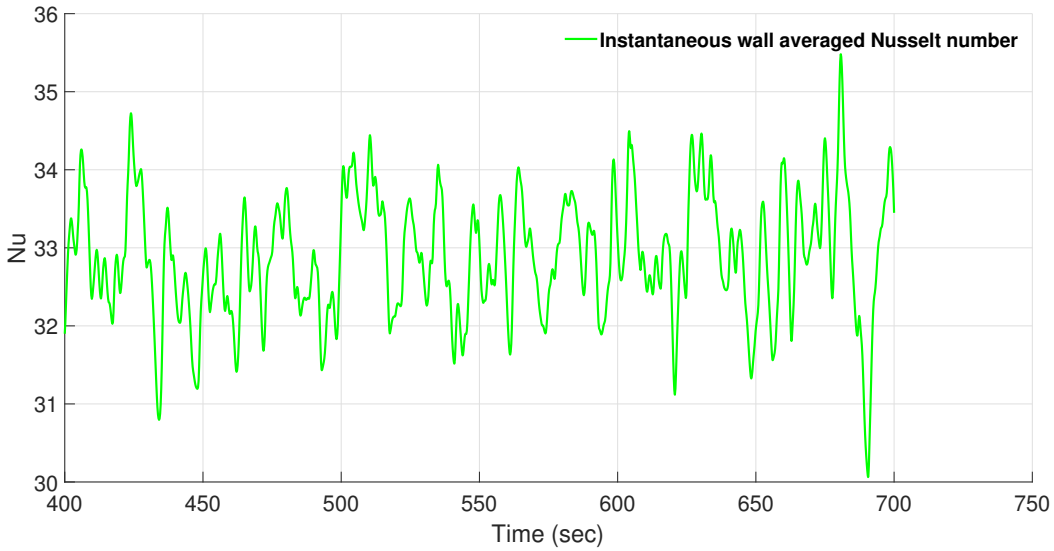

(b) Instantaneous wall averaged Nusselt number.

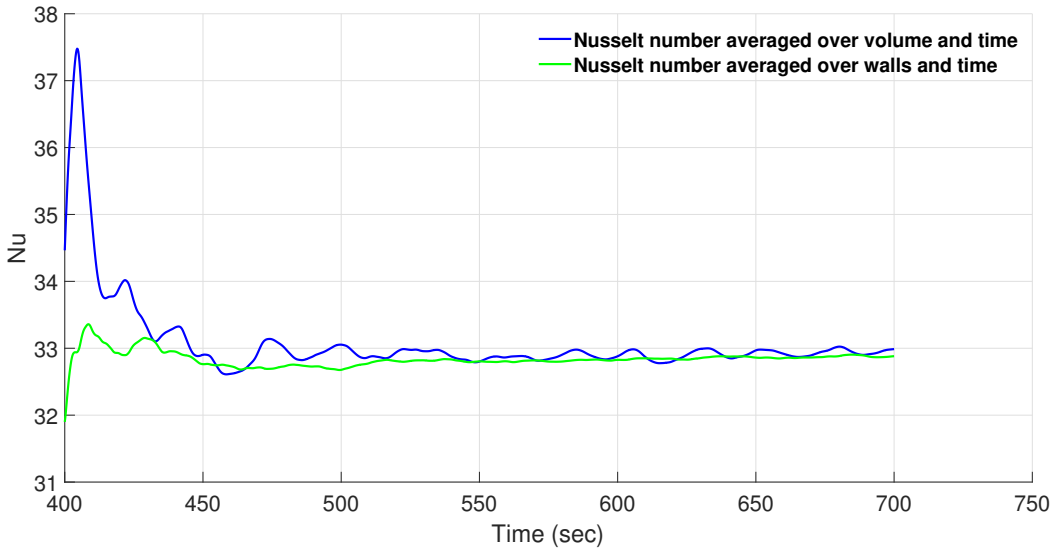

(c) Time averaged Nusselt number's convergence

Figure 7.8: Plots of computed wall and volume averaged Nusselt number for Ra = 10^8.

As discussed in the Section 7.6, the wall averaged and the volume averaged Nusselt numbers are computed using the Equations (7.3) and (7.4) respectively. The Figures 7.7a and 7.8a shows the computed instantaneous volume averaged Nusselt number for the Ra = 10^6 and 10^8 respectively. Similarly, Figures 7.7b and 7.8b shows the computed instantaneous wall averaged Nusselt number for the Ra = 10^6 and 10^8 respectively. The volume averaged Nusselt number computation requires a correct estimation of the fluctuations in the bulk for evaluating the $u_z T$ term, see Equation (7.3). Whereas the wall averaged expression requires an adequate spatial resolution for the thermal boundary layer. With the increase in Ra the heat transfer and hence the Nu will increase. For higher Ra (10^8), the thermal plumes are smaller and due to higher intensity of flow movement, more turbulent mixing of the flow will occur resulting in higher heat transfer.

The Figures 7.7c and 7.8c show the convergence of the time averaged Nusselt numbers obtained from the two expressions for Ra = 10^6 and 10^8 respectively. It can be observed that the volume averaged Nusselt number requires longer duration for convergence and that is because of the large-scale fluctuations in the bulk's mean temperature.

After an adequate time duration the Nusselt number computed from the both expression converges to the same value. For the agreement of the two expressions, it is necessary to well resolve the flow in both bulk and in the boundary layers. Therefore, from the results obtained it can be concluded that the spatial resolution used for the simulations was adequate.

7.8. Discussion of results.

The work of the Kooij et al. performed using Nek500, which is considered for the validation in this project, is concerned about scaling of heat transfer with Rayleigh Number for the rotating RBC. However, cases with non-rotating RBC were also studied for the comparison. Since, we are interested in the DNS of the PTS with buoyancy effects which involves stationary geometry, the results of non-rotating RBC formed the basis for the validation in this project.

The time-averaged Nusselt number from the two expressions, 7.4 and 7.3, for all the cases performed by Kooij et al. are given in the Figure 7.9. The Rossby number, Ro, of 0.9 and ∞ corresponds to rotating and stationary RBC case respectively. The result of the cases (with Ro = ∞) for different Rayleigh numbers, i.e, $10^6 and 10^8$, performed in this project and in the Kooij et al. work are compared in the Table 7.3.

Ra	*Ro*	$\langle Nu \rangle_W$	$\langle Nu \rangle_V$
10^6	0.09	5.7 ± 0.2	5.5 ± 0.2
10^6	∞	9.0 ± 0.1	9.0 ± 0.1
10^7	0.09	16.0 ± 0.3	16.1 ± 0.5
10^7	0.36	18.8 ± 0.1	18.8 ± 0.4
10^7	1.08	17.3 ± 0.1	17.4 ± 0.3
10^7	∞	16.4 ± 0.1	16.5 ± 0.2
10^8	0.09	37.9 ± 0.3	38.2 ± 0.8
10^8	∞	33.0 ± 0.1	33.2 ± 0.4
10^9	0.09	72.2 ± 0.5	73.8 ± 1.0
10^9	0.36	71.2 ± 0.2	72.2 ± 0.9
10^9	1.08	66.8 ± 0.2	67.0 ± 1.6
10^9	∞	64.5 ± 0.3	66.5 ± 1.8

Figure 7.9: Time-averaged Nusselt number, including 95% confidence bounds for Pr = 6.4, Γ =1 for varying Ro and Ra, adopted from [10].

Rayleigh number	**Validation Work**			**Kooij et al. study**		
	$< Nu >_v$	$< Nu >_w$	Simulation time	$< Nu >_v$	$< Nu >_w$	Simulation time
$Ra = 10^6$	8.1	8.1	650 sec	9.0 $\pm$ 0.1	9.0 $\pm$ 0.1	300 sec
$Ra = 10^8$	32.9	33.0	700 sec	33.0 $\pm$ 0.1	33.2 $\pm$ 0.4	300 sec

Table 7.3: Comparison of the simulations result with Kooij et al. results.

A considerable difference between the computed and Kooij et al. work's Nusselt number for the case with Ra = 10^6 was observed. However, the results for the case with Ra = 10^8 are matching with an insignificant difference. The difference for the case with Ra = 10^6 can be attributed to the simulation and averaging time because mesh resolution and simulation setup were similar for both the studies. The Kooij et al. used a total simulation time of 300 seconds and averaging time of last 200 seconds whereas here, a simulation time of 650 seconds and averaging time of 150 seconds was considered. Moreover, it was observed that the volume averaged number is fluctuating till longer time duration in the case of Ra = 10^6, which indicates towards the requirement of longer simulation time. Since the flow scenario in the case with Ra = 10^6 is characterised by the larger thermal plumes and their movement in the bulk, the volume averaged Nusselt number shows higher fluctuation and require larger time duration for the convergence. In contrast, the Ra = 10^8 is characterised by smaller and less coherent thermal plumes which result in faster effective heat transfer and eventually reaching the steady state earlier.

8

Summary and Conclusions

This thesis project concerns a phenomenon that occurs in a nuclear reactor called pressurised thermal shock (PTS), which is identified as one of those nuclear reactor's safety issue where CFD can provide more insight and can prove to be a useful predictive method. A direct numerical simulation (DNS) can form a reference database to validate the turbulence modelling CFD methodologies and can help in overcoming some of the limitation of the past experimental studies of the PTS. The spectral element method based Nek5000 solver is selected to perform this DNS. Since performing a DNS requires huge computational resources and time, it is necessary that the simulation case is feasible for the DNS and at the same time incorporates all the important aspects of the phenomenon of interest. Therefore, an extensive preliminary study is performed in this thesis project for the high-fidelity DNS of the single-phase PTS scenario with buoyancy effects.

As the first task, a numerical case is designed for the single-phase PTS scenario, with emphasis on the buoyancy driven flow mixing in the downcomer. The buoyancy driven flow was simulated by using Boussinesq approximation with the unsteady incompressible Navier-Stokes equations. Since the flow mixing is a transient phenomenon, time evolution of the flow properties are studied. With the help of several simulations the physical domain, boundary conditions and flow parameters are calibrated individually to find the optimum ones. After finalising the optimum geometrical dimensions and boundary conditions, length scales study is performed which will help in an approximate estimation of the mesh, for the DNS, and identifying the critical regions that requires mesh refinement.

As the second task, an assessment of Nek5000 is carried out with a buoyancy driven flow mixing test case. Since the PTS case involves complex geometry with large computational time requirements, it becomes essential to perform a validation study with a smaller test case in prior to the simulation of the PTS case. For this purpose, a DNS of Rayleigh Bénard convection (RBC) is performed with Nek5000 code and the results are compared with the past work of Kooij et al. [10]. Two simulations with Rayleigh number (Ra) of 10^6 and 10^8 were performed with a similar simulation setup as used by Kooij et al. in their work. A good agreement was observed with the Nusselt number calculations, and the characteristics of flow topology is found to be similar as observed in the past experimental and numerical studies of RBC. However, considerable difference in the Nusselt number computation was observed with the Ra = 10^6 case and this difference can be attributed to the smaller computational and averaging time used by Kooij et al. The RBC case involves buoyancy driven flow mixing scenario where the flow movement is result of density difference generated due to the heat transfer. In this validation study, the Boussinesq approximation with unsteady incompressible Navier-Stokes equation is used and therefore, the similar implementation can be used for the DNS of PTS case.

There is still some recommendation of other studies which can be performed in future, before the final DNS of the PTS case. The RBC validation study performed in this thesis project is a case of natural convection, where there is no inflow or outflow through the domain, unlike the PTS case. Therefore, a case of forced convection in a rectangular channel with inflow and outflow can be studied.

Bibliography

[1] B. L. Smith, *Assessment of CFD codes used in nuclear reactor safety simulations,* Nuclear Engineering and Technology **42**, 339 (2010).

[2] S. Kliem, T. Sühnel, U. Rohde, T. Höhne, H.-M. Prasser, and F.-P. Weiss, *Experiments at the mixing test facility ROCOM for benchmarking of CFD codes,* Nuclear Engineering and Design **238**, 566 (2008).

[3] D. Häfner *et al.*, *HDR safety program—thermal mixing in the cold leg and downcomer of the HDR test rig,* Report PHDR , 91 (1990).

[4] D. C. Wilcox *et al.*, *Turbulence modeling for CFD*, Vol. 2 (DCW industries La Canada, CA, 1998).

[5] J. H. Ferziger and M. Peric, *Computational methods for fluid dynamics* (Springer Science & Business Media, 2012).

[6] P. Fischer, J. Lottes, S. Kerkemeier, O. Marin, K. Heisey, A. Obabko, E. Merzari, and Y. Peet, *NEK5000: User's manual*, Tech. Rep. (Technical Report ANL/MCS-TM-351, Argonne National Laboratory, 2015).

[7] P. F. Fischer, *An overlapping Schwarz method for spectral element solution of the incompressible Navier-Stokes equations,* Journal of Computational Physics **133**, 84 (1997).

[8] A. Shams, G. Damiani, D. Rosa, and E. Komen, *Design of a single-phase PTS numerical experiment for a reference direct numerical simulation,* Nuclear Engineering and Design **300**, 282 (2016).

[9] R. Verzicco and R. Camussi, *Numerical experiments on strongly turbulent thermal convection in a slender cylindrical cell,* Journal of Fluid Mechanics **477**, 19 (2003).

[10] G. L. Kooij, M. Botchev, and B. J. Geurts, *Direct numerical simulation of Nusselt number scaling in rotating Rayleigh Bénard convection,* International journal of heat and fluid flow **55**, 26 (2015).

[11] K. Kang and L. Kupca, *Pressurised thermal shock in nuclear power plants: Good practices for assessment,* Handbook on deterministic evaluation for the integrity of reactor pressure vessel, IAEA TECDOC-1627, IAEA, Vienna (2010).

[12] I. N. E. Series, *Integrity of reactor pressure vessels in nuclear power plants: assessment of irradiation embrittlement effects in reactor pressure vessel steels.*, Tech. Rep. (NP, 2009).

[13] C. Jang, *Treatment of the thermal–hydraulic uncertainties in the pressurized thermal shock analysis,* Nuclear engineering and design **237**, 143 (2007).

[14] T. Theofanous, H. Nourbakhsh, P. Gherson, and K. Iyer, *Decay of buoyancy driven stratified layers with applications to pressurized thermal shock (PTS).[PWR]*, Tech. Rep. (Purdue Univ., Lafayette, IN (USA). School of Nuclear Engineering, 1984).

[15] T. Tlieofaiious and U. Nourbaklish, *PWR downcomer fluid temperature transients due to high pressure injection at stagnated loop flow,* in *Joint NRC/ANS Meeting on Basic Thermal Hydraulic Mechanisms in LWR Analysis* (1982) pp. 583–613.

[16] H.-M. Prasser, G. Grunwald, T. Höhne, S. Kliem, U. Rohde, and F.-P. Weiss, *Coolant mixing in a pressurized water reactor: deboration transients, steam-line breaks, and emergency core cooling injection,* Nuclear Technology **143**, 37 (2003).

[17] U. Rohde, T. Höhne, S. Kliem, B. Hemström, M. Scheuerer, T. Toppila, A. Aszodi, I. Boros, I. Farkas, P. Mühlbauer, *et al.*, *Fluid mixing and flow distribution in a primary circuit of a nuclear pressurized water reactor— validation of CFD codes,* Nuclear Engineering and Design **237**, 1639 (2007).

[18] S. M. Willemsen and E. Komen, *Assessment of RANS CFD modelling for pressurized thermal shock analysis,* in *Proceedings of the 11th International Topical Meeting on Nuclear Reactor Thermal-Hydraulics (NURETH-11)* (2005).

[19] M. Loginov, E. Komen, and A. Kuczaj, *Application of large-eddy simulation to pressurized thermal shock problem: A grid resolution study,* Nuclear Engineering and Design **240**, 2034 (2010).

[20] A. N. Kolmogorov, *The local structure of turbulence in incompressible viscous fluid for very large Reynolds numbers,* in *Dokl. Akad. Nauk SSSR*, Vol. 30 (1941) pp. 299–303.

[21] A. Kolmogorov, *Energy dissipation in locally isotropic turbulence,* in *Dokl. Akad. Nauk SSSR*, Vol. 32 (1932) pp. 9–21.

[22] F. T. Nieuwstadt, J. Westerweel, and B. J. Boersma, *Turbulence: introduction to theory and applications of turbulent flows* (Springer, 2016) pp. 12–15.

[23] P. K. Kundu, I. M. Cohen, D. R. Dowling, P. S. Ayyaswamy, and H. H. Hu, *Fluid mechanics*, 5th ed. (Elsevier Academic Press, Waltham :, 2012).

[24] R. Kunnen, B. J. Geurts, and H. Clercx, *Experimental and numerical investigation of turbulent convection in a rotating cylinder,* Journal of fluid mechanics **642**, 445 (2010).

[25] W. Jones and B. Launder, *The prediction of laminarization with a two-equation model of turbulence,* International journal of heat and mass transfer **15**, 301 (1972).

[26] H. Tennekes and J. L. Lumley, *A first course in turbulence* (MIT press, 1972).

[27] G. E. Karniadakis, M. Israeli, and S. A. Orszag, *High-order splitting methods for the incompressible Navier-Stokes equations,* Journal of computational physics **97**, 414 (1991).

[28] G. Ahlers, S. Grossmann, and D. Lohse, *Heat transfer and large scale dynamics in turbulent Rayleigh-Bénard convection,* Reviews of modern physics **81**, 503 (2009).

[29] E. D. Siggia, *High Rayleigh number convection,* Annual review of fluid mechanics **26**, 137 (1994).

[30] B. Castaing, G. Gunaratne, F. Heslot, L. Kadanoff, A. Libchaber, S. Thomae, X.-Z. Wu, S. Zaleski, and G. Zanetti, *Scaling of hard thermal turbulence in Rayleigh-Bénard convection,* Journal of Fluid Mechanics **204**, 1 (1989).

[31] R. M. Kerr, *Rayleigh number scaling in numerical convection,* Journal of Fluid Mechanics **310**, 139 (1996).

[32] F. Chillà and J. Schumacher, *New perspectives in turbulent Rayleigh-Bénard convection,* The European Physical Journal E: Soft Matter and Biological Physics **35**, 1 (2012).

[33] X.-D. Shang, X.-L. Qiu, P. Tong, and K.-Q. Xia, *Measured local heat transport in turbulent Rayleigh-Bénard convection,* Physical review letters **90**, 074501 (2003).

[34] R. Togni, A. Cimarelli, and E. De Angelis, *Physical and scale-by-scale analysis of Rayleigh-Bénard convection,* Journal of Fluid Mechanics **782**, 380 (2015).

[35] O. Reynolds, *On the dynamical theory of incompressible viscous fluids and the determination of the criterion.* Proceedings of the Royal Society of London **56**, 40 (1894).

A

Appendix

A.1. Reynolds averaging

The averaging concept introduced by Reynolds [35] has three forms, i.e. time, spatial, and ensemble averaging which are used for the turbulence related studies. Based on the type of turbulence behaviour of flow these averaging schemes are used.

Time averaging is useful for stationary turbulence, a turbulent flow which on average does not vary with time, and is expressed as :

$$F_T(x) = \lim_{T\to\infty} \frac{1}{T} \int_{t+T}^{t} f(x,t)dt, \tag{A.1}$$

where instantaneous flow variables is represented by f(x,t) and its time average by $F_T(x)$.

Spatial averaging is used for the homogeneous turbulence where the flow, in average, is uniform in all directions. Here a volume integral is taken over all spatial coordinates as expressed below :

$$F_V(t) = \lim_{V\to\infty} \frac{1}{V} \iiint f(x,t)dV. \tag{A.2}$$

Ensemble averaging is best suited for the turbulent flows that decay in time. Here the averaging is done based on the sample set of N identical experiments where f(x,t) = $f_n(x,t)$ in the n^{th} experiment, the average, F_E, is expressed as

$$F_E(x,t) = \lim_{N\to\infty} \frac{1}{N} \sum_{n=1}^{N} .f_n(x,t) \tag{A.3}$$

As most of the flow problems involve inhomogeneous turbulence, time averaging is preferred form of Reynolds averaging.

A.2. Statistics

The turbulent flows are random and unsteady in nature and it is not necessary to study all the details of the flow for most applications. The statistical quantities like average and standard deviation of flow variable can provide the required insight about the flow. Reynolds [35] suggested the decomposition of instantaneous velocity into the components of mean and fluctuation as a representation of turbulent flows. The underlying idea is that most of the turbulent flows have reproducible averages and the averages are more of practical interest than fluctuations. The expression representing the instantaneous velocity, u_i is:

$$u_i(x,t) = U_i(x) + u_i'(x,t), \tag{A.4}$$

where U_i and u_i' is the mean and fluctuating part respectively. The above expression is commonly known as Reynolds decomposition. In the following discussion the time average will be denoted by an overbar ($\overline{x}$) and fluctuation will be denoted by prime (x').

These are some important Reynolds conditions which result into following relationships: $\overline{u}' = 0$, $\overline{\overline{u}} = \overline{u}$, and $\overline{\overline{f}\,\overline{g}} = \overline{f}\,\overline{g}$

A.3. Correlation

On time averaging the product of two properties, which can be decomposed into mean and fluctuation, the product of the mean and the fluctuation will have a zero mean. Therefore, only two terms with product of mean and fluctuation will remain, as follows:

$$\overline{\phi\kappa} = \overline{\phi\kappa + \phi\kappa' + \phi'\kappa + \phi'\kappa'} = \overline{\phi}\,\overline{\kappa} + \overline{\phi'\kappa'}. \tag{A.5}$$

This forms the basis in deriving the RANS equation which is obtained by substituting the mean and fluctuation of velocity in the NS equation and taking the time average of it.

A.4. Reynolds stress transport (RST) equation

To find the equation for stress tensor, the moment of NS equation is taken. That is the NS equation is multiplied by a fluctuating property and then the product is time averaged. This results into Reynolds stress transport (RST) equation:

$$\frac{\partial \tau_{ij}}{\partial t} + U_k \frac{\partial \tau_{ij}}{\partial x_k} = -\tau_{ik}\frac{\partial U_j}{\partial x_k} - \tau_{jk}\frac{\partial u_i}{\partial x_k} + \epsilon_{ij} - \Pi_{ij} + \frac{\partial}{\partial x_k}[\nu\frac{\partial \tau_{ij}}{\partial x_k} + C_{ijk}]. \tag{A.6}$$

Each term of the RST equation has physical significance. The description is discussed for each term.
Advection : transport by mean flow

$$K_{ij} = U_k \frac{\partial \tau_{ij}}{\partial x_k}. \tag{A.7}$$

Production : increase of turbulence intensity by energy transfer from the mean flow.

$$P_{ij} = -\tau_{ik}\frac{\partial U_j}{\partial x_k} - \tau_{jk}\frac{\partial u_i}{\partial x_k}. \tag{A.8}$$

Dissipation : dissipation into thermal energy.

$$\epsilon_{ij} = 2\nu\overline{\frac{\partial u_i'}{\partial x_j}\frac{\partial u_j'}{\partial x_i}}. \tag{A.9}$$

Pressure strain correlation : redistribution of energy among components

$$\Pi_{ij} = \overline{\frac{p'}{\rho}(\frac{\partial u_i'}{\partial x_j} + \frac{\partial u_j'}{\partial x_i})}. \tag{A.10}$$

Diffusion that includes viscous diffusion : transport by viscous stress, turbulent diffusion : transport by turbulence, and pressure diffusion : transport by pressure fluctuations

$$\rho C_{ijk} = \overline{\rho u_i' u_j' u_k'} + \overline{p' u_i'}\delta_{jk} + \overline{p' u_j'}\delta_{ik}. \tag{A.11}$$

The solution of nonlinear NS equations for turbulent flow will result into complex solutions and with ever higher moment, additional unknowns will be generated. Therefore, turbulence modelling is required to devise approximations for the unknown correlations with the help of known flow properties.

A.5. Turbulence kinetic energy

An important measure of the turbulent flow is the intensity of turbulent fluctuations. This is measured in terms of Reynolds stress components $\overline{u'^2}$, $\overline{v'^2}$, $\overline{w'^2}$. Turbulent kinetic energy (k) is defined as

$$k = \frac{1}{2}(\overline{u'^2} + \overline{v'^2} + \overline{w'^2}) = \frac{1}{2}\overline{u_i' u_i'}. \tag{A.12}$$

.

A.6. Eddy viscosity hypothesis

Turbulence leads to the momentum exchange between fluid elements. Boussinesq postulated that the Reynolds stress tensor, τ_{ij}, is proportional to the mean shear rate, S_{ij}. The proportionality factor is eddy viscosity, μ_τ. The relation is expressed as :

$$\tau_{ij} \cong 2\mu_T S_{ij} - \frac{2}{3}\delta_{ij}k \tag{A.13}$$

where, k is Turbulent kinetic energy, δ_{ij} is Kronecker delta which is given by

$$\delta_{ij} = \begin{cases} 1 & \text{if i = j} \\ 0 & \text{if i } \neq \text{j} \end{cases}, \tag{A.14}$$

and mean shear rate tensor, S_{ij}, is expressed as

$$S_{ij} = \frac{1}{2}\left(\frac{\partial \overline{u}_i}{\partial x_j} + \frac{\partial \overline{u}_j}{\partial x_i}\right) - \frac{1}{3}\delta_{ij}\frac{\partial \overline{u}_k}{\partial x_k}. \tag{A.15}$$

This hypothesis forms the basis for all the one equation and two equation turbulence models like $k-\epsilon$ and $k-\omega$.

A.7. Turbulent kinetic energy equation

As discussed earlier, the turbulent kinetic energy (TKE) is expressed as one half of Reynolds stress tensor. The transport equation for k can be obtained from Reynolds transport equation by writing it according to definition of k. The TKE equation is given as :

$$\rho\frac{\partial k}{\partial t} + \rho U_j\frac{\partial k}{\partial x_j} = \tau_{ij}\frac{\partial U_i}{\partial x_j} - \rho\epsilon + \frac{\partial}{\partial x_j}\left[(\mu + \mu_T/\sigma_k)\frac{\partial k}{\partial x_j}\right]. \tag{A.16}$$

.

A.8. Nek5000

NeK5000 is a higher order method based computational fluid dynamics open-source code, developed at Argonne laboratories in Chicago. It is written in Fortran, F77, and C and is based on highly scalable spectral element method. It is capable of parallel processing by dividing the calculation to multiple processor using MPI and therefore, well suitable for the DNS.